

© 2009 David Michael Mahr

THREE-DIMENSIONAL, IN-SILICO BREAST PHANTOM FOR
MULTIMODALITY IMAGE SIMULATIONS

BY

DAVID MICHAEL MAHR

THESIS

Submitted in partial fulfillment of the requirements
for the degree of Master of Science in Bioengineering
in the Graduate College of the
University of Illinois at Urbana-Champaign, 2009

Urbana, Illinois

Adviser:

Michael F. Insana

Abstract

We report on the construction of anatomically realistic three-dimensional *in-silico* breast phantoms with adjustable sizes, shapes and morphologic features. The concept of multiscale spatial resolution is implemented for generating breast tissue images from multiple modalities. Breast epidermal boundary and subcutaneous fat layer is generated by fitting an ellipsoid and 2nd degree polynomials to reconstructive surgical data and ultrasound imaging data. Intraglandular fat is simulated by randomly distributing and orienting adipose ellipsoids within a fibrous region immediately within the dermal layer. Cooper's ligaments are simulated as fibrous ellipsoidal shells distributed within the subcutaneous fat layer. Individual ductal lobes are simulated following a random binary tree model which is generated based upon probabilistic branching conditions described by ramification matrices, as originally proposed by Bakic et al [3,4]. The complete ductal structure of the breast is simulated from multiple lobes that extend from the base of the nipple and branch towards the chest wall. As lobe branching progresses, branches are reduced in height and radius and terminal branches are capped with spherical lobular clusters. Biophysical parameters are mapped onto the complete anatomical model and synthetic multimodal images (Mammography, Ultrasound, CT) are generated for phantoms of different adipose percentages (40%, 50%, 60%, and 70%) and compared against clinical examples. Analytic methods applied to compare synthetic with clinical images. Results demonstrate that the *in-silico* breast phantom has applications in imaging performance evaluation and, specifically, great utility for solving image registration issues in multimodality imaging.

To my mom and dad for all of their love and support throughout my education.

Acknowledgments

This project would not have been possible without the support and guidance of many people. Thank you to my adviser, Michael Insana, for providing guidance, the opportunity to work with you, and being a mentor to me. Thank you to Rohit Bhargava for help and expertise with many aspects of the work. Thanks to the Beckman Institute at the University of Illinois for providing the financial means to complete this project. Finally, thank you to all of my family and friends for all of their support and encouragement throughout my education.

Table of Contents

Acknowledgments	iv
List of Tables	vii
List of Figures	viii
Chapter 1 Introduction	1
Chapter 2 Anatomical Research	3
2.1 Breast Overview	3
2.2 Breast Boundary	4
2.3 Subcutaneous Fat Layer and Fibroglandular Region	6
2.4 Subcutaneous-Fibrous Surface	7
2.5 Intraglandular Fat and Cooper's Ligaments	8
2.6 Ductal Structure	8
2.7 Pectoral Muscle, Chest Wall & Vasculature	10
2.8 Breast Phantoms from Literature	11
2.9 Phantom Overview	12
Chapter 3 Methods	15
3.1 Phantom Simulation	15
3.1.1 Primary Objects	15
3.1.2 Secondary Objects	23
3.1.3 Ductal Structure	30
3.1.4 Complete Phantom	44
3.2 Visualization	46
3.2.1 Mapping Object Space to Phantom Space	47
3.2.2 Discretization and Tissue Assignment	48
Chapter 4 Results	54
4.1 Image Modality Simulations	54
4.2 Mammography	54
4.2.1 Mammography Simulation	54
4.2.2 Mammography Analysis	56
4.3 Ultrasound	60
4.3.1 Ultrasound Simulation	60
4.3.2 Ultrasound Analysis	61
4.4 Computed Tomography	64
4.4.1 Computed Tomography Simulation	64
4.4.2 Computed Tomography Analysis	64
Chapter 5 Discussion	68
5.1 Strengths, Weaknesses and Future Developments	68

References	73
----------------------	----

List of Tables

2.1	Anthropomorphic Measurements	5
2.2	Tissue Thickness Percentages	7
3.1	Outer Boundary Reference Points	17
3.2	Inner Boundary Reference Points	22
3.3	Ductal Opening Locations and Initial Branch Directions	40
4.1	Mass Attenuation Coefficients and Densities	55
4.2	Fractal Dimension Results	59
4.3	Clinical and Simulated Fractal Dimension Results from Literature	60
4.4	Acoustic Impedance Values	60

List of Figures

2.1	Breast Anatomy Overview	4
2.2	Anthropomorphic Measurement Points	5
2.3	Ultrasound Scan Locations	6
2.4	Cumulative Tissue Depths	7
2.5	Ductal System Reconstructions	10
2.6	Phantom Structure Overview	13
3.1	Tissue Regions/Layers	15
3.2	Ellipsoidal Reference Points	17
3.3	Ellipsoidal and Upper Attachment Point Sets	19
3.4	Upper and Lower Breast Boundary Sections	21
3.5	Retromammary Fat Layer	22
3.6	Subcutaneous Fat Layer and Fibroglandular Tissue Region	23
3.7	Subcutaneous-Fibrous Surface Illustration	23
3.8	Subcutaneous-Fibrous Surface Simulations	25
3.9	Ellipsoid Characteristics	26
3.10	Intraglandular Fat Illustration	26
3.11	Adipose Percentage Data	27
3.12	Intraglandular Fat Generation Flowchart	28
3.13	Intraglandular Fat Simulations	28
3.14	Cooper's Ligaments Illustration	29
3.15	Cooper's Ligaments Simulation	30
3.16	Labeled Binary Trees	32
3.17	Random Binary Tree Generation	34
3.18	Random Binary Tree Examples	35
3.19	Physical Characteristics of Ductal Branches	36
3.20	Ductal Tree with/without Height and Radius Variance	37
3.21	Lobe Axis and Lobe Angle Examples	38
3.22	Branching Angles Illustration	38
3.23	Ductal Opening Locations	40
3.24	Starting Ductal Branches	41
3.25	Ductal Structure Illustration	41
3.26	Ductal Tree Generation Flowchart	43
3.27	Lobule Illustration	44
3.28	Ductal Tree with/without Lobules	44
3.29	Ductal Structure Simulation	44
3.30	Complete Phantom Generation Flowchart	45
3.31	Visualization Overview	47
3.32	Mapping from Object to Phantom Space	48
3.33	1D Mapping Example	49
3.34	2D Discretization Example	50

3.35	2D Mapping and Discretization Example	51
3.36	Mapping and Discretization Overview	53
4.1	Optical Density Characteristic Curve	57
4.2	Mammography Simulation Results	58
4.3	Fractal Analysis Diagram	59
4.4	Ultrasound Simulation Example	61
4.5	Ultrasound Simulation Results	62
4.6	CT Simulation Diagram	65
4.7	CT Simulation Results	66

Chapter 1

Introduction

The following project proposes the construction of a three-dimensional in-silico breast phantom for multimodality imaging. The breast phantom is constructed using mathematical models to simulate structures within the breast derived from anatomical data gathered from the literature and other previous work. Once the mathematical models are generated, a three-dimensional software phantom of user set dimensions and resolution is mapped and discretized into a matrix. Simulated images are produced by processing the phantom using image acquisition system models for mammography, ultrasound, and computed tomography.

Anatomical research on breast anatomy has been limited since Sir Astley Cooper's pioneering work documented in *The Anatomy and Disease of the Breast* in 1845 until some relatively recent studies [9]. In Cooper's work, many different structures of the breast were identified and categorized through dissection including ductal networks, fibrous, glandular, and adipose tissue distribution, Cooper's ligaments, and several others. While these structures had been identified, detailed anatomical metrics of these structures were not available until recently. Further anatomical research of these structures has been performed through the use of microdissection, histology, and imaging techniques. The thickness of tissue layers, intraglandular fat composition, ductal branching, breast shape, and many other structures have been characterized through these methods and reported. As a result of these studies, more anatomical information of the breast is available. These details prove useful in the generation of our breast model.

Phantoms are objects that are imaged by imaging systems to assess system performance. For instance, phantoms can be used for the testing of new processing algorithms and imaging techniques. A phantom can be constructed to analyze specific imaging characteristics (i.e. resolution, contrast, etc), or can be *anthropomorphically* constructed to mimic the anatomical features of part of a human or biological subject. An anthropomorphic hardware phantom is used with hardware imaging systems and is typically an object consisting of different materials chosen to interact with energies of the imaging modality similar to that of actual tissue. These materials are constructed

in such a way to mimic anatomical distributions of tissues. An anthropomorphic software or *in-silico* phantom exists in software and can be used with software-based imaging system simulators to generate simulated images. For our case, we focus on the construction of an anthropomorphic three-dimensional software phantom to model the breast.

There has primarily been two different approaches to generating software breast phantoms in recent studies. One of these methods is to assign tissue types to voxels using segmented imaging data [18]. The other approach is generating mathematical models to simulate structures of the breast using anatomical data and then assigning tissue types to voxels [1,5]. The latter method allows for scalable dimensions and resolution ideal for multimodality simulation, as well as user adjustment of structures for variable phantom generation (i.e. variable tissue compositions, randomization). For these reasons, we use the mathematical modeling method to generate our phantom.

There are many advantages and uses for our multimodality software phantom. Contrary to a hardware phantom or an actual subject, the software phantom offers high repeatability because the position, orientation, and environment are controlled. Additionally, the original object function being imaged is known thus the location of specific structures is retrievable. These properties are important for applications such as multimodality image registration.

The software phantom also provides a rapid and inexpensive method for image generation. Using an image simulator, new image processing algorithms and imaging techniques can be quickly simulated and system performance can be assessed. Using a hardware phantom and imaging system, testing can be slow and expensive. The software phantom offers a rapid method of validating new processing algorithms and techniques before testing on actual imaging hardware. The use of a software phantom for simulation can potentially greatly reduce the time and cost of imaging system development.

Building upon anatomical data in literature and past software phantoms, a method for generated a three-dimensional software phantom of the breast for the use of multimodality imaging simulation is proposed. The goal of developing a breast phantom for multimodality imaging will hopefully provide a valuable tool for advancing and developing the areas and applications presented.

Chapter 2

Anatomical Research

The goal of the software phantom is to construct mathematical models that closely resemble and follow known anatomical data. To find such data, anatomical texts and recent research articles were sought out and the most applicable information was compiled. While research on breast anatomy has been limited until recent studies, much more detail about the anatomy and organization of tissue has been documented and quantitated [4,10,13,17,19,23,24,26,27]. In instances of contradicting results, the best inference was made to determine how the software phantom should model a particular structure. Upon completion of the anatomical investigation, metrics to be used for the different structural models of the phantom are determined.

2.1 Breast Overview

The breast is primarily composed of adipose, fibrous, and glandular tissues that are positioned over the pectoral muscle of the chest wall. The structures that make up the breast are illustrated in Figure 2.1. The outermost layer of the breast is the skin layer. The skin layer includes the epidermis and dermis that function as a protective layer. Immediately beneath the skin is the subcutaneous fat layer. The subcutaneous fat layer is primarily made up of adipose tissue and extends throughout the outer boundary of the breast. The retromammary fat layer extends along the pectoral muscle and is of the same tissue consistency as subcutaneous fat. For the purposes of our study, we included both the subcutaneous fat layer and retromammary fat layer in the classification of the subcutaneous fat layer. The subcutaneous fat layer (including the retromammary fat layer) encompasses the fibroglandular tissue region within the inner region of the breast. The fibroglandular region is primarily made up of fibrous tissue in addition to containing the glandular tissue of the ductal structure. The ductal structure is composed of lobules and ducts that are responsible for milk production and transportation to the nipple, respectively. Additionally within the fibroglandular region are small volumes of intraglandular fat. The breast is attached to the body via the pectoral

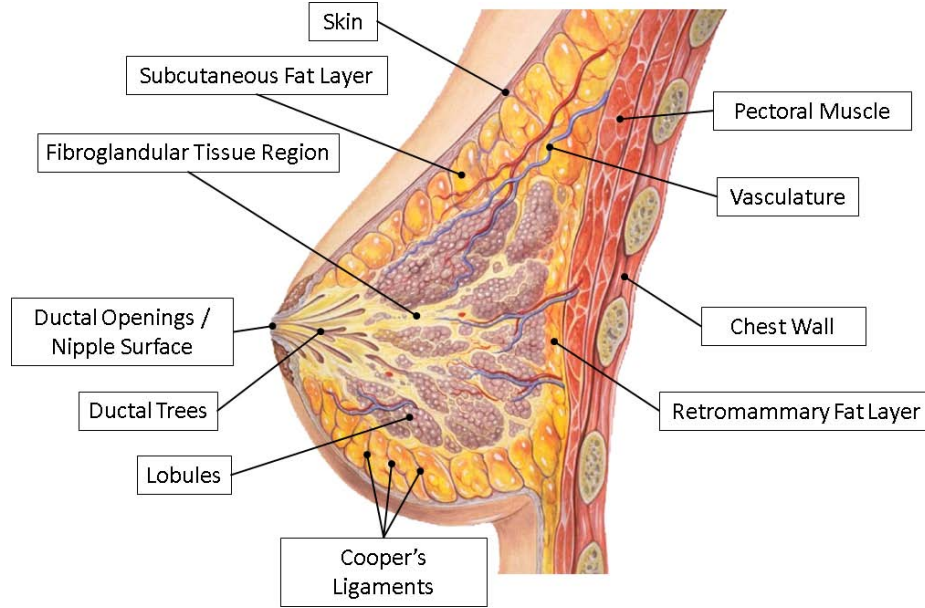


Figure 2.1: Breast anatomy illustration. Skin, subcutaneous fat layer, and fibroglandular tissue region make up the different layers/regions of the breast from outer to innermost. The entire breast structure is attached to the body at the pectoral muscle. Ductal trees and lobules make up the glandular tissue of the breast. Cooper's ligaments are fibrous elements that are responsible for breast structure and attachment to the pectoral muscle. (Illustrated by and adapted with permission from Patrick J. Lynch)

muscle that lies against the chest wall. Cooper's ligaments exist within the subcutaneous fat layer and are small ligaments of fibrous tissue. Cooper's ligaments attach the fibroglandular region to the skin and pectoral muscle in order to define the breast structure and attach the breast to the body.

2.2 Breast Boundary

External dimensions of the breast are compiled from several anatomical studies related to plastic surgery. A study by Westreich et al recorded anthropomorphic breast measurements from fixed skeletal points of 50 women [32]. In a study by Vandeput et al, similar anthropomorphic measurements were taken from 973 women [31]. Another anatomical study by Rusby et al calculated mean nipple measurements from 25 subjects [27]. Measurements useful to our breast phantom include: sternum to nipple, nipple to inframammary crease, nipple diameter, breast width and breast projection length. Locations of these measurements are illustrated in Figure 2.2. The breast width measurements are interpreted and estimated from the actual results in the studies, as the breast width measurement was measured differently in the studies than the defined measurement in Figure 2.2. Measurements are compared between each study and appropriate dimensions for our phantom

are determined as shown in Table 2.1.

Additional information is provided in a study by Catanuto et al that performed breast shape analysis [8]. The study evaluated the curvature of the breast at different regions where curvature values ranged from -0.2 to 0.2. Curvature is a metric used to measure how an object deviates from being flat where positive curvature is spheroid-like, negative curvature is hyperboloid-like, and curvature of zero indicates a flat region. The results show that the curvature of the breast below the nipple is positive and becomes flat above the nipple. The study also demonstrated that the breast begins to run parallel to the rest of the chest at a distance halfway towards the clavicle. This information is used in determining the boundary points of the phantom.

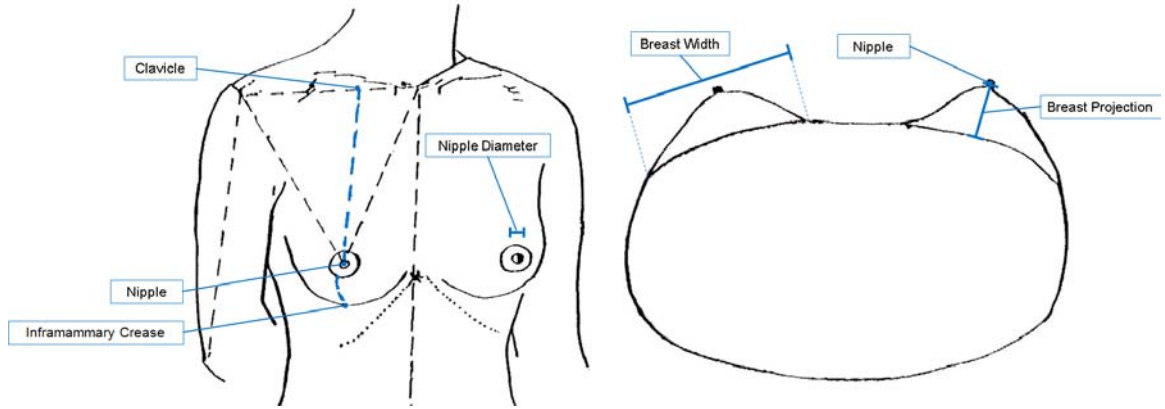


Figure 2.2: Anthropomorphic measurement points used to help define phantom size. Measurement values are shown in Table 2.1. (Figure is adapted with permission from Westreich et al [32].)

Anthropomorphic Measurements

<i>Measurement</i>	<i>Study #1 [32]</i>	<i>Study #2 [31]</i>	<i>Study #3 [27]</i>	<i>Interpreted Value</i>
Nipple-Clavicle	18.80 cm	20.96 cm	-	19.88 cm
Nipple-Inframammary Crease	6.90 cm	7.33 cm	-	7.12 cm
Nipple Diameter	-	-	1.2 cm	1.2 cm
Breast Projection	4.93 cm	-	-	4.93 cm
Breast Width	12.67 cm	-	-	12.67 cm

Table 2.1: Anthropomorphic measurements for studies by Westreich et al (Study #1), Vandeput et al (Study #2), and Rusby et al (Study #3) [27,31,32]. The interpreted values are determined from the results in each study and are used in our phantom study.

2.3 Subcutaneous Fat Layer and Fibroglandular Region

The subcutaneous fat layer encompasses the fibroglandular tissue region where the subcutaneous fat layer contains mostly adipose tissue and the fibroglandular tissue region contains mostly fibrous and glandular tissue. The subcutaneous fat layer thickness is relatively constant throughout the breast boundary, however it is thinner in close proximity to the nipple. The retromammary fat layer thickness is also relatively constant as it extends over the pectoral muscle. However, it is important to note that the thickness of both layers varies from subject to subject based on body mass index (BMI) and other factors. In a study by Ramsay et al, ultrasound images were used to calculate the cumulative axial tissue thicknesses for each breast of 21 lactating women [26]. Ultrasound images were taken at multiple locations along eight different radial axes as shown in Figure 2.3. The thickness percentages of each tissue measured (subcutaneous fat, intraglandular fat, retromammary fat, and fibroglandular tissue) were calculated and the results are provided in Table 2.2. Additionally, detailed tissue thicknesses for two women were provided for scans at different radial distances from the nipple (Figure 2.4). It is important to note that studies have shown that a lactating breast typically exhibits an increase in fibroglandular to fat ratio compared to non-lactating, where a lactating breast has approximately a 2:1 ratio as opposed to 1:1 for the non-lactating case [19]. These metrics are used to determine the structure and thickness of the subcutaneous and retromammary fat layers in our phantom and help define the fibroglandular tissue region.

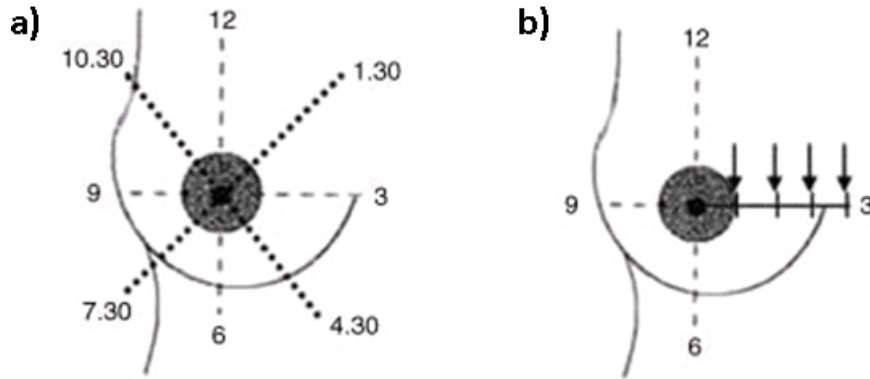


Figure 2.3: Ultrasound scans were taken along the radial lines shown in (a) at 3 cm intervals extending from the nipple shown in (b). Intervals continued to the end of each breast. (Figure used with permission from Ramsay et al [26].)

Tissue Thickness Percentages	
<i>Tissue Type</i>	<i>Thickness Percentage</i>
Subcutaneous Fat	23%
Intraglandular Fat	6.5%
Retromammary Fat	8%
Total Fat Tissue	37.5%
Fibrous/Glandular Tissue	62.5%

Table 2.2: Thickness percentages of tissues averaged over multiple scans at different radial located positions (Figure 2.3) on lactating breasts [26]. It is important to note that lactating breasts exhibit a 2:1 fibroglandular to fat ratio compared to 1:1 for non-lactating.

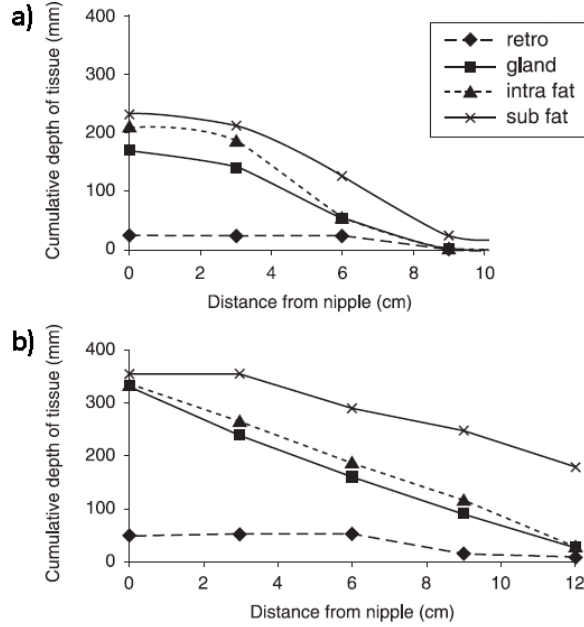


Figure 2.4: Results from scans of two different women. The graphs show the cumulative tissue thicknesses for multiple radial intervals along from the breast. 8 scans were summed at each interval, where each scan is made at the same interval along a different radial axis as shown in Figure 2.3. (Figure used with permission from Ramsay et al [26].)

2.4 Subcutaneous-Fibrous Surface

Because the subcutaneous fat layer and fibroglandular region consist of different tissues, there is an interface or surface between the two regions. Medical imaging has shown that the surface between the two layers is irregular as opposed to smooth. Research evaluating the statistics or metrics of the subcutaneous-fibrous surface is non-existent. However, hardware breast phantoms for ultrasound have been created using different methods to simulate the subcutaneous fat layer in two different studies by Madsen et al [20,21]. In one study, a layer of tissue-mimicking spheres of 13 mm diameter were used to simulate the subcutaneous fat layer and surface [21]. In another study, a subcutaneous fat layer mold was created by milling a mold surface with a sphere of 3 cm diameter at random

locations and depths [20]. Therefore, a similar method is used to define the surface model in our phantom.

2.5 Intraglandular Fat and Cooper’s Ligaments

Intraglandular fat is adipose tissue that exists within the fibroglandular region of the breast. The amount of intraglandular fat is dependent on the BMI of the individual and other factors [10, 23]. Studies have also shown that there is a positive correlation to the amount of intraglandular fat and both increasing age and increasing breast size [10, 17]. The adipose percentage of the breast is a metric of measuring fat content and is defined as the sum of both subcutaneous and intraglandular fat volumes divided by the total breast volume. In a study by Lee et al, the adipose percentages of 40 women were estimated using mammograms and breast MRI [17]. The results found the mean adipose percentage of these individuals to be $66.5\% \pm 18\%$. Medical images have shown that intraglandular fat typically exists as small, elongated compartments, however limited research exists related to the metrics of these adipose compartments. Previous software phantom studies have attempted to model these compartments using spheres ranging in size from 2.7 to 5.3 mm radius [1]. These metrics are used as a reference to help model intraglandular fat in our phantom.

Cooper’s ligaments are fibrous elements that exist within the subcutaneous and retromammary fat layers. They function as connective tissue to support and connect the fibroglandular region to the skin and the pectoral muscle. This provides the breast its structure and attachment to the body. Limited research exists related to the structure of Cooper’s ligaments. Medical images have shown that Cooper’s ligaments typically exist as fibrous tissue shells encompassing adipose tissue and extending from the fibroglandular region towards the skin and pectoral muscle. The software phantom by Bakic et al modeled Cooper’s ligaments as spherical shells ranging in sizes from 5.3 to 13.3 mm radius whose centers were randomly distributed within the subcutaneous fat layer [1]. The software phantom by Bliznakova et al simulated Cooper’s ligaments as ellipsoidal shells with center points randomly distributed within the subcutaneous fat layer [5]. These methods and metrics are used to help define the structural model of Cooper’s ligaments within our phantom.

2.6 Ductal Structure

The ductal structure exists within the fibroglandular region. Typical descriptions of breast anatomy divide the ductal structure into 15-25 lobes or sections within the fibroglandular region [11–13, 19].

Within each lobe exists a ductal tree which is a network of connecting ductal branches that begin at the nipple. At the ends of these ductal trees are lobules that function to produce milk, while the ductal tree functions to drain the lobules to the nipple. There are typically 5-9 ductal openings that can be identified at the nipple surface [28]. The nipple diameter (area that can contain ductal openings) ranges from 1 to 2.5 cm [25, 32]. It is generally believed that ductal trees merge into larger ducts that eventually converge into several main ducts near the nipple that open to ductal openings [19]. This helps explain reasoning for the discrepancy between the number of ductal openings and lobes.

Ductal trees are composed of a network of ductal branches. Main ducts are ductal branches that initiate at ductal openings at the nipple and extend into the fibroglandular region. Main ducts then branch into a series of lactiferous ducts, which continue to branch to form the ductal tree structure. Eventually branching stops at branches called terminal ductal branches.

Located at the terminal branch ends of ductal trees are lobules. Each lobule is a cluster of 10-100 alveoli or acini that are approximately 0.12 mm in diameter [19]. The software phantom by Bliznakova et al modeled lobules as 1 mm diameter spheres [5]. A similar method is incorporated into our phantom.

Ductal openings are very small, ranging from 0.10 to 1.5 mm in diameter with a majority lying between 0.38 and 0.75 mm diameter [28]. Near the ductal opening, main duct radii are initially very small as well at 0.4 to 0.7 mm diameter [10]. The diameter of main ducts increases to 1.3 to 2.7 mm as they extend farther away from the nipple [26]. The length of main ducts before the first branch is approximately 8.2 ± 6.27 mm [26]. Lactiferous duct radii and height decrease as their degree of branching within the ductal tree increases. While limited research on the size of lactiferous ducts exists, phantom studies have typically modeled ductal trees to follow organic tree models in that each branch maintains a relatively constant radius:height ratio [3, 5].

Until recently, detailed knowledge of the ductal structure was limited. However, two different studies by Going et al and Ohtake et al used histological slices to reconstruct complete three-dimensional models of the breast ductal structure [13, 24]. These studies reveal that lobes overlap with one another and that ductal tree branches intertwine with one another, like roots of a tree. Figure 2.5 shows the reconstructed three-dimensional ductal structure models generated in these two different studies. The ductal structure exists exclusively within the fibroglandular region with the brief exception of main ducts passing through the subcutaneous fat layer from ductal openings.

The branching nature of the ductal structure was analyzed by Bakic et al by examining galac-

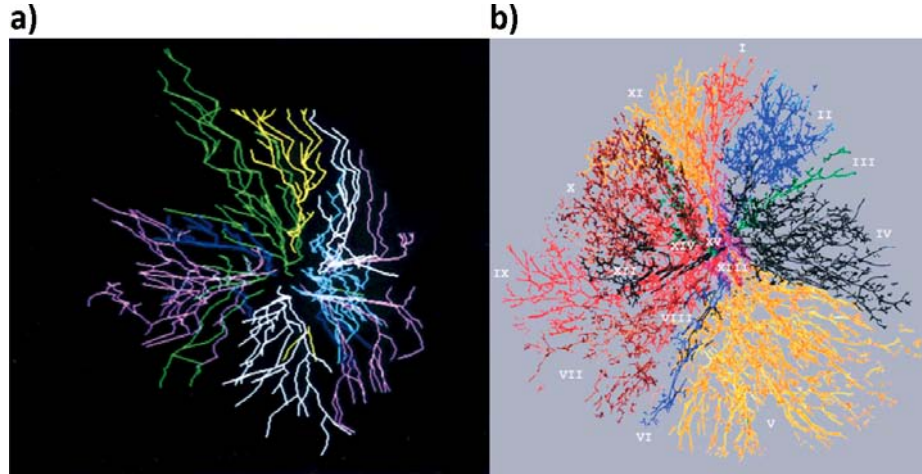


Figure 2.5: Three-dimensional ductal structures reconstructed from histological slices of the breast in two different studies by (a) Ohtake et al and (b) Going et al [13,24]. It is important to note that while ductal trees are separate structures, they can overlap each other. (Figure used with permission from Ohtake et al and Going et al [13,24].)

tograms [3,4]. A galactogram is a mammogram with dye injected into a ductal opening to produce contrast within a single ductal tree. By tracing galactograms to map out individual ductal trees, branching probabilities were calculated by assuming a random binary tree model. The results of this study are described in more detail in the Methods chapter and are used to help develop our phantom ductal structure.

2.7 Pectoral Muscle, Chest Wall & Vasculature

The pectoral muscle is situated on the upper anterior of the chest wall and lies directly underneath the breast. The attachment of the pectoral muscle to the breast and chest wall is responsible for breast attachment to the body. The size of the muscle is dependent on the subject. The pectoral muscle and chest wall define the posterior boundary of the breast and is used as the posterior boundary of our phantom as well.

The blood supply of the breast is provided by the anterior and posterior medial branches of the internal mammary artery and lateral mammary branch of the lateral thoracic artery [10]. Smaller sources include the posterior intercostal arteries and the pectoral branch of the thoracoacromial artery. Venous drainage is composed of a deep drainage system and superficial drainage system. Both systems drain into the internal thoracic, axillary, and cephalic veins. Deep veins are assumed to follow the inner mammary artery, while the superficial veins consist of subareola veins that branch radially from the nipple and drain into the periareolar vein. The periareolar vein circles the nipple

and connects both the deep and superficial systems. The blood supply and vasculature is highly variable between women. Additionally, the vasculature structure does not appear to be associated with the ductal structure. For the scope of this project, the vasculature is ignored in our phantom.

2.8 Breast Phantoms from Literature

While some basic, low anatomical detailed software breast phantoms have been developed previously, it was not until recently that higher anatomically detailed software phantoms were produced. Three different breast phantoms closely related to our work are examined and used as reference for methods of generating our phantom. These phantoms are created by Bakic et al, Bliznakova et al, and Li et al.

The phantom created by Bakic et al is a three-dimensional breast phantom designed for mammogram simulation [1–3]. The phantom is constructed simulating large to medium scale tissue structures using mathematical models. These structures include the breast boundary, subcutaneous fat layer, fibroglandular region, intraglandular fat, Cooper’s ligaments, and the ductal structure. The breast boundary is simulated by an ellipsoid and similarly the subcutaneous fat layer and fibroglandular region are defined by an inner ellipsoid. The intraglandular fat and Cooper’s ligaments are simulated using small adipose spheres and fibrous spherical shells. The ductal structure is generated as a network of cylinders following anatomically measured branching probabilities. To generate a simulated mammogram, the phantom is subjected to a compression model to estimate breast deformation using tissue elasticity parameters. Next, the X-ray image acquisition process is modeled for a monochromatic parallel beam. Simulated mammograms are validated through fractal analysis and resulting fractal dimensions are compared to clinical results.

The phantom created by Bliznakova et al is also a three-dimensional breast phantom designed for mammogram simulation [5]. The construction is similar in that mathematical models are used to simulate the anatomical structures of the breast. These structures include the breast boundary, Cooper’s ligaments, ductal structure and mammographic background. The subcutaneous fat layer, fibroglandular region, and intraglandular fat are indirectly defined by the other structures. The breast boundary is defined by a lower ellipsoid and upper hyperboloid. Cooper’s ligaments are simulated using fibrous ellipsoidal shells containing adipose tissue that are placed near the breast boundary surface, indirectly defining the subcutaneous fat layer and fibroglandular region. The ductal structure is generated similarly as a network of cylinders following anatomically measured

branching probabilities. The main difference between the phantom by Bakic et al and Bliznakova et al is how each phantom generates the mixture of adipose and fibrous tissue within the fibroglandular region. While Bakic et al explicitly models these structures as adipose spheres, Bliznakova et al generates a “mammographic background texture” to simulate the texture commonly associated with mammograms. Using fractal methods to generate this three-dimensional mammographic background, mammographic texture can be generated for x-ray acquisition simulation. Simulated mammograms are validated through visual comparison with clinical images using independent observers. While this method provides seemingly better mammographic image results, it lacks the ability to be used with other imaging modalities. For this reason, we choose to model all structures explicitly.

A phantom created by Li et al uses an inverse approach to generate the software phantom [18]. CT image data of a breast is segmented to identify different tissues and tissue densities of the breast, including adipose and fibrous tissue. Using these classifications, voxels of the three-dimensional phantom are then assigned specific tissue types and tissue densities at locations equivalent to those within the segmented CT data. Using the generated breast phantom, image acquisition simulations are used to produce simulated mammograms and breast CT images. Simulated mammograms are validated using similar fractal analysis techniques and simulated CT images are validated through visual comparison with clinical CT images.

2.9 Phantom Overview

Anatomical studies provide detailed information about the breast and its organization of tissue. The goal of our phantom simulation is to create a three-dimensional model of the breast that follows known anatomical data. Here, we break the breast anatomy into separate distinct structures: Breast boundary, subcutaneous fat layer, fibroglandular tissue region, subcutaneous-fibrous surface, intraglandular fat, Cooper’s ligaments, and ductal structure including ducts and lobules. Mathematical models are used to construct each structure using geometric objects. Each model is designed using anatomical knowledge to support its construction. In some areas, research relating to a specific structure is limited, thus some inferences using biological knowledge are made to interpret how to model the structure. As anatomical detail of these different structures reveals itself through further research, we would be able to improve the modeling method. This would be a continuous area of improvement for our software phantom.

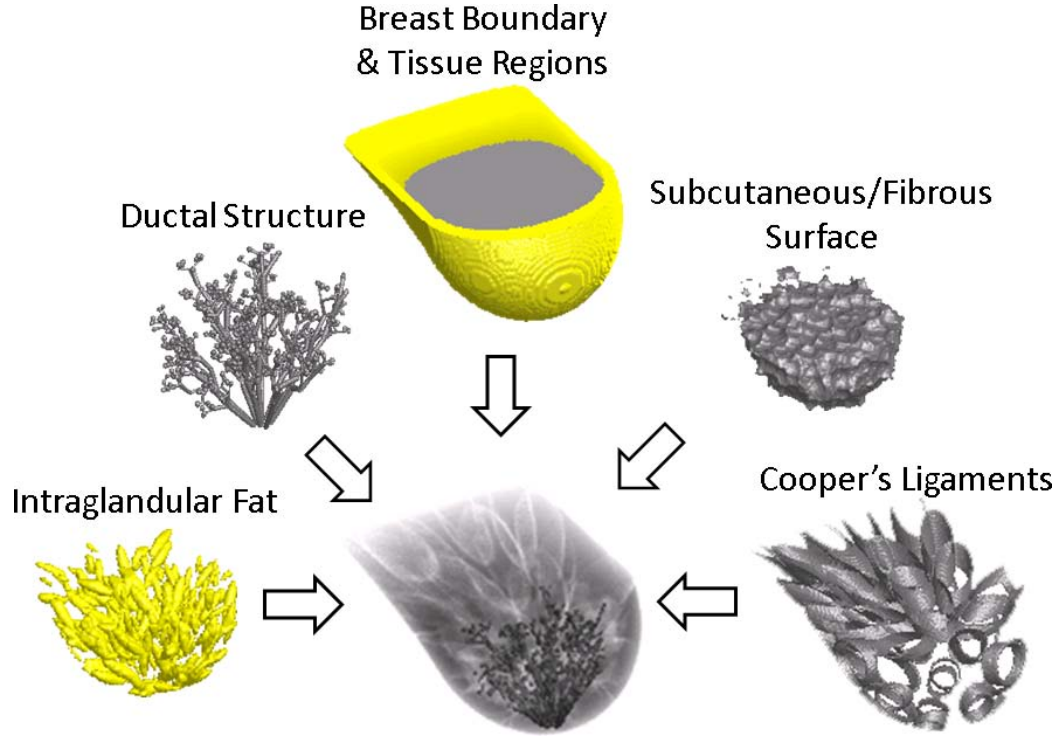


Figure 2.6: Structures that compose the complete breast phantom. Structures include the breast boundary, tissue regions (subcutaneous fat layer and fibroglandular region), subcutaneous-fibrous surface, intraglandular fat, Cooper's ligaments and ductal structure.

Each structural model is defined by an array of geometric descriptions defining the size and spatial locations of the various geometric objects that construct each structure. When generating the complete breast phantom, the volume dimensions and resolution desired for the phantom are specified and these geometric descriptions are used to construct the volume within these constraints as a discrete matrix volume. This is done as opposed to mapping each structure directly to a discrete matrix volume because geometric descriptions of each model maintain the continuous measurements and allows dynamic scalability. This dynamic scalability allows a breast volume to be regenerated for various dimensions and resolutions using the same models. Thus, the phantom maintains the same overall structure while visualizing any volume dimensions and resolution.

The breast volume is created by *mapping* each of these structures onto the same continuous three-dimensional axis and then *discretizing* the continuous three-dimensional structures onto a discrete three-dimensional matrix, where each element or voxel represents a specific tissue type as shown in Figure 2.6. There are three tissue types used in our breast phantom including adipose, fibrous, and glandular tissues, and each structure consists of at least one of these tissue types. The tissue type assigned to each voxel is determined by the tissue assignment conditions of the geometric objects

for each structure. If a voxel is determined to be within the boundaries of a geometric object of a structure, it is assigned to represent that object's tissue type. After all structures have been mapped and discretized into the three-dimensional matrix, the complete phantom volume is constructed and is ready for further processing.

Chapter 3

Methods

3.1 Phantom Simulation

Structures are categorized into sections: Primary objects, secondary objects, and ductal structure. Primary objects are large scale objects relating to tissue regions. Secondary objects are medium scale objects that reside within the primary object regions. Ductal structure corresponds to the ductal trees and lobules of the breast. The proceeding describes the generation of each of these structures in detail.

3.1.1 Primary Objects

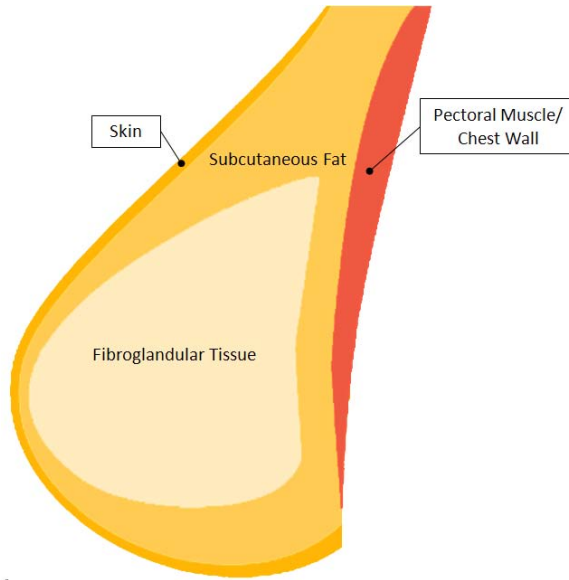


Figure 3.1: Illustration of subcutaneous fat layer, fibroglandular region, pectoral muscle, chest wall and skin layer.

The breast consists of several layers of tissue. The outermost tissue layer is the skin layer, which consists of the epidermis and dermis layers. Immediately beneath the skin layer is the subcutaneous

fat layer that primarily consists of adipose tissue. Also included in the definition of the subcutaneous fat layer is the retromammary fat layer that extends along the pectoral muscle. Enclosed by the subcutaneous fat layer is the fibroglandular region that primarily consists of fibrous and glandular tissue. The pectoral muscle is located at the posterior of the breast and extends along the chest wall. These layers/regions are illustrated in Figure 3.1.

For our purposes, we ignore the skin layer (epidermis and dermis) and use the pectoral muscle as the posterior boundary of our phantom. To simulate each region, an ellipsoid and 2nd degree polynomials are used. Anatomical data is used to best fit the ellipsoid and polynomials to model the boundary of each region. These regions are the base level of anatomical detail and are deemed *primary objects*.

Outer Boundary

The breast is defined on a three-dimensional set of axes (x -, y -, and z -axis). The depth dimension of the breast is defined by the z -axis. The chest wall located in the $z = 50$ mm plane and is called the *chest wall plane*, while the nipple is located in the $z = 0$ mm plane. The vertical dimension of the breast is defined by the y -axis where lower values correspond to distal points on the breast and higher values correspond to proximal points on the breast. The lateral dimension of the breast is defined by the x -axis, where lower values correspond to the left side and higher values correspond to the right side.

The outer breast boundary is defined by a three-dimensional ellipsoid and series of 2nd degree polynomials. The ellipsoid and 2nd degree polynomials are designed to fit reference points that are user defined on the outer surface, with the ellipsoid defining the lower part of the breast and polynomials defining the upper part. These reference points are determined using the anthropomorphic measurements from Table 2.1 and breast curvature information from Section 2.2 [8,31,32].

Six spatial reference points are determined to fit the ellipsoid and are shown in Figure 3.2: Nipple point, lower attachment point, left attachment point, right attachment point, lower breast point, and upper ellipsoid point. The nipple is the most outward point of the breast and is positioned to be 50 mm from the chest wall, approximately the measured breast projection length, and lies in the $z = 0$ mm plane. The lower attachment point is located in the chest wall plane and is positioned slightly below the height of the nipple. The left and right attachment points are both located in the chest wall plane, are positioned at the same height as the nipple, and are on symmetrical sides of the breast. The distance between each attachment point is calculated to be 80 mm, approximately the

interpreted breast width distance. The lower breast point is used to help define the lower curvature of the breast. It is located below the nipple, and at depth halfway between the chest wall and nipple. The upper ellipsoid point is used to define the upper bounds of the ellipsoid and maintain curvature. It is positioned in the chest wall plane at a height approximately halfway between the upper attachment line segment of the breast (discussed later) and the nipple. The exact locations of these reference points are provided in Table 3.1 and illustrated in Figure 3.2.

Outer Boundary Reference Points

<i>Label</i>	<i>Reference Point</i>	<i>Coordinates</i>	<i>Spatial Locations (mm)</i>
P1	Nipple Point	(x_0, y_0, z_0)	(50,50,0)
P2	Lower Attachment Point	(x_1, y_1, z_1)	(50,34,50)
P3	Left Attachment Point	(x_2, y_2, z_2)	(10,50,50)
P4	Right Attachment Point	(x_3, y_3, z_3)	(90,50,50)
P5	Lower Breast Point	(x_4, y_4, z_4)	(50,25,25)
P6	Upper Ellipsoid Point	(x_5, y_5, z_5)	(50,110,50)
@ P1	Nipple Tangent Slope	$\frac{\partial z}{\partial y}$	0

Table 3.1: Outer boundary reference points and slope used as input to fit ellipsoid.

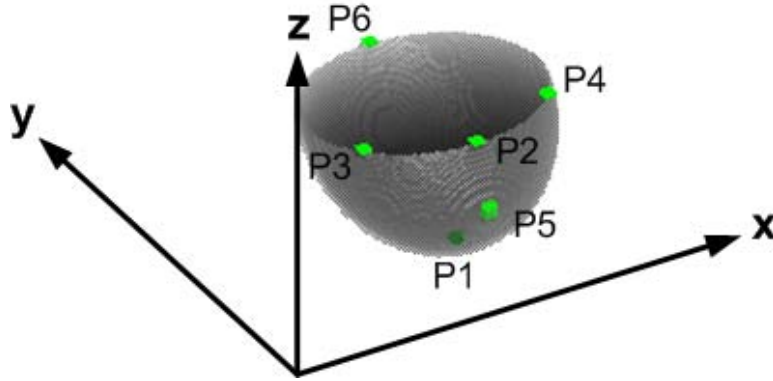


Figure 3.2: Ellipsoid fit to reference points.

To fit an ellipsoid to these reference points, we first must define the ellipsoid equation. The general equation for an ellipsoid is

$$Ax^2 + By^2 + Cz^2 + Dxy + Exz + Fyz + Gx + Hy + Iz = 1. \quad (3.1)$$

However, we are restricting the ellipsoid to be symmetrical over the yz -plane that passes through the nipple. Because of this restriction, the D and E terms will be equal to zero, thus we can ignore them. Rewriting Equation 3.1, we have

$$Ax^2 + By^2 + Cz^2 + Fyz + Gx + Hy + Iz = 1. \quad (3.2)$$

Here, we have seven unknowns, therefore to define the ellipsoid, we need seven solutions. We have six reference points, thus we need an additional constraint to solve. Additionally, we define the tangent slope of the ellipsoid at the nipple to be equal to zero, or $\frac{\partial z}{\partial y} = 0$. This ensures that the nipple is the outermost point of the breast. For this constraint, we must take the partial derivatives of Equation 3.2 with respect to y and z , and then solve for $\frac{\partial z}{\partial y}$.

Taking the partial derivative of Equation 3.2 with respect to y we have

$$2By\partial y + Fz\partial y + H\partial y = 0. \quad (3.3)$$

Similarly, taking the partial derivative with respect to z we have

$$2Cz\partial z + Fy\partial z + I\partial z = 0. \quad (3.4)$$

Combining each, we can derive $\frac{\partial z}{\partial y}$ as

$$2By\partial y + Fz\partial y + H\partial y = 2Cz\partial z + Fy\partial z + I\partial z, \quad (3.5)$$

$$\partial y(2By + Fz + H) = \partial z(2Cz + Fy + I), \quad (3.6)$$

$$\frac{\partial z}{\partial y} = \frac{2By + Fz + H}{2Cz + Fy + I}. \quad (3.7)$$

Because we are solving for $\frac{\partial z}{\partial y} = 0$, we can simply solve for

$$2By + Fz + H = 0. \quad (3.8)$$

We now have seven equations and seven solutions. We can solve for the unknowns by setting up the equations in matrix form as

$$\begin{bmatrix} 1 \\ 1 \\ 1 \\ 1 \\ 1 \\ 1 \\ 0 \end{bmatrix} = \begin{bmatrix} x_0^2 & y_0^2 & z_0^2 & y_0 z_0 & x_0 & y_0 & z_0 \\ x_1^2 & y_1^2 & z_1^2 & y_1 z_1 & x_1 & y_1 & z_1 \\ x_2^2 & y_2^2 & z_2^2 & y_2 z_2 & x_2 & y_2 & z_2 \\ x_3^2 & y_3^2 & z_3^2 & y_3 z_3 & x_3 & y_3 & z_3 \\ x_4^2 & y_4^2 & z_4^2 & y_4 z_4 & x_4 & y_4 & z_4 \\ x_5^2 & y_5^2 & z_5^2 & y_5 z_5 & x_5 & y_5 & z_5 \\ 0 & 2y_0 & 0 & z_0 & 0 & 1 & 0 \end{bmatrix} \begin{bmatrix} A \\ B \\ C \\ F \\ G \\ H \\ I \end{bmatrix}$$

By inverting the matrix, we can then solve for the unknowns in Equation 3.2 to define the outer boundary ellipsoid.

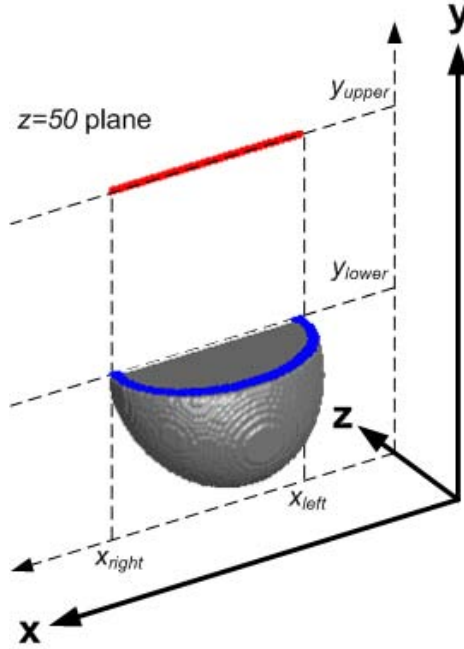


Figure 3.3: 2nd degree polynomials define the upper half of the phantom by joining upper attachment point (red) and ellipsoidal attachment points (blue) where $y_{\text{upper}} = 160$ mm and $y_{\text{lower}} = 20$ mm.

The upper part of the outer boundary is simulated using 2nd degree polynomials joining a set of upper breast attachment points and set of points on the ellipsoid. Literature has shown that the breast curvature is positive (rounded) in the lower half of the breast, gradually becomes more flat just above the nipple, and begins to run parallel to chest wall approximately halfway between the clavicle and nipple [8]. The *upper attachment set* of points is defined as a line segment that lies in the chest wall plane ($z = 50$ mm plane) at height $y_{\text{upper}} = 160$ mm. This height is approximately equal to half of the nipple-to-clavicle distance above the nipple (110 mm). The line segment extends

parallel to the x-axis from either side of the breast width and is shown in Figure 3.3 as the red line segment. The *ellipsoidal set* of points are defined by the points on the ellipsoid that lie in the xz -plane at $y_{\text{lower}} = 20$ mm, taken to be approximately the same height above the nipple as the lower breast point is below the nipple to maintain curvature. The ellipsoidal set of points is shown in Figure 3.3 as the blue segment. The 2nd degree polynomials joining these two point sets are modeled as

$$y = Az^2 + Bz + C \quad (3.9)$$

where A , B , and C are unknown. The polynomials are defined in the yz -plane, thus points of both sets are paired together that lie in the same yz -plane. The upper attachment points and ellipsoidal points are referred to as (x_u, y_u, z_u) and (x_e, y_e, z_e) respectively. To maintain continuity, the tangent slope of the ellipsoid in the yz -plane, $\frac{\partial y_e}{\partial z_e}$ is calculated at each ellipsoidal set point and is used as a third constraint to the 2nd degree polynomial equation. The method for calculating $\frac{\partial y_e}{\partial z_e}$ for a given point on the ellipsoid can be found by simply inverting the result we found in Equation 3.7. The resulting equation is

$$\frac{\partial y_e}{\partial z_e} = \frac{2Cz_e + Fy_e + I}{2By_e + Fz_e + H} \quad (3.10)$$

where x_e , y_e , and z_e correspond to a point within the ellipsoidal set. This slope is used to solve for the derivative of Equation 3.9 with respect to z derived as

$$\frac{\partial y}{\partial z} = 2Az + B. \quad (3.11)$$

Using the pair of points, and the tangent slope at the ellipsoidal set point, the 2nd degree polynomial unknowns can be solved for by setting up the equations in matrix form as

$$\begin{bmatrix} y_e \\ y_u \\ \frac{\partial y_e}{\partial z_e} \end{bmatrix} = \begin{bmatrix} z_e^2 & z_e & 1 \\ z_u^2 & z_u & 1 \\ 2z_e & 1 & 0 \end{bmatrix} \begin{bmatrix} A \\ B \\ C \end{bmatrix}$$

The solution can then be solved by inverting the matrix. By applying this solution to all pairs of points, a complete set of polynomials can be found to define the upper part of the breast boundary. Thus, the *lower part* of the breast is defined by the ellipsoid for $y < 20$ mm and the *upper part* of the breast is defined by the polynomials for $y \geq 20$ mm as shown in Figure 3.4.

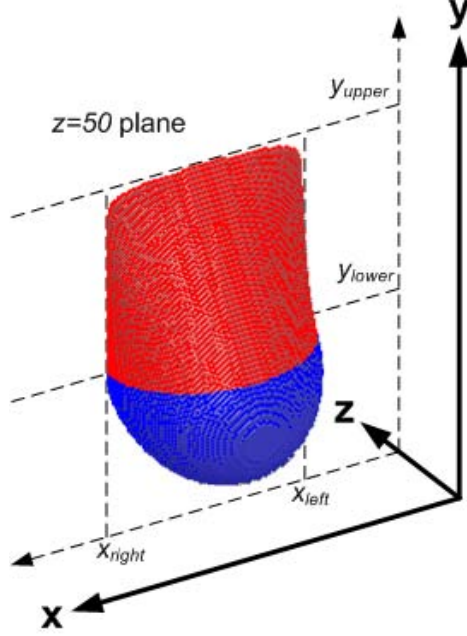


Figure 3.4: The outer boundary of the breast is defined by an ellipsoid in the lower part (blue) and by 2nd degree polynomials in the upper part (red) where $y_{upper} = 160$ mm and $y_{lower} = 20$ mm.

Inner Fibroglandular Region

In our simulation, the inner fibroglandular region is defined by a similar, yet smaller inner boundary located within the outer boundary. The inner boundary is defined by the same number of spatial reference points that are selected inside the outer boundary. These points are selected based on anatomical data that describes the thickness of the subcutaneous fat tissue at various points within the breast. A study by Ramsay et al uses ultrasound imaging to calculate the cumulative axial tissue thicknesses within the breast of subcutaneous fat, intraglandular fat, retromammary fat, and fibroglandular tissue [26]. Using the data from Table 2.2 and Figure 2.4 in Section 2.3, we can select how far inward to define the inner boundary reference points. The average thickness percentage of subcutaneous fat tissue for various locations in the breast is approximately 23%. This is also supported with the case study results in Figure 2.4, with the exception of scans located near the nipple. Thus, we can define the inner boundary points to be approximately 23% inward from the corresponding outer boundary points, with the exception of the nipple point. By examining the case studies in Figure 2.4, we can define the inner boundary nipple point to be approximately 7.5% inward from the outer boundary nipple point. The inner boundary reference points and slope are defined in Table 3.2.

Additionally, the upper attachment set of points for the inner boundary is shifted inward by

Inner Boundary Reference Points

<i>Label</i>	<i>Reference Point</i>	<i>Coordinates</i>	<i>Spatial Locations (mm)</i>
Q1	Nipple Point	(x_0, y_0, z_0)	(50,50,4)
Q2	Lower Attachment Point	(x_1, y_1, z_1)	(50,26,50)
Q3	Left Attachment Point	(x_2, y_2, z_2)	(19,50,50)
Q4	Right Attachment Point	(x_3, y_3, z_3)	(81,50,50)
Q5	Lower Breast Point	(x_4, y_4, z_4)	(50,19,25)
Q6	Upper Ellipsoid Point	(x_5, y_5, z_5)	(50,96,50)
@ Q1	Nipple Tangent Slope	$\frac{\partial z}{\partial y}$	0

Table 3.2: Inner boundary reference points and slope used as input to fit ellipsoid (where Q1 is equivalent to P1, etc.).

approximately 23%, while the ellipsoidal attachment set of points height is kept the same, resulting in $y_{\text{upper}} = 135$ mm and $y_{\text{lower}} = 20$ mm. The inner boundary is fit to an ellipsoid and 2nd degree polynomials in the exact same manner as the outer boundary.

Retromammary Fat Layer

The retromammary fat layer extends along the pectoral muscle, posterior to the fibroglandular region. The retromammary fat layer has relatively constant thickness (Figure 2.4). Using results from Table 2.2 and Figure 2.4 in Section 2.3, we can define the retromammary layer to have a thickness of 4 mm. This thickness layer extends over the posterior side of the inner fibroglandular region. The retromammary layer is incorporated into the outer boundary and subcutaneous fat layer as shown in Figure 3.5. We define the retromammary fat layer to be part of the subcutaneous fat layer.

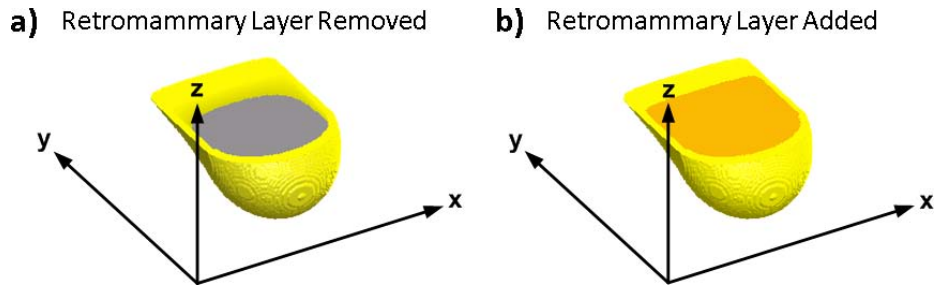


Figure 3.5: The retromammary fat layer is located between the fibroglandular region and chest wall: Shown removed in (a) and shown in orange in (b). For considerations of our phantom, the retromammary fat layer is defined to be included in the subcutaneous fat layer.

The *subcutaneous fat layer* is designated as the volume between the outer and inner boundaries and is assigned as adipose tissue, while the *fibroglandular region* is designated as the volume inside the inner boundary and is assigned as fibrous tissue. The retromammary fat layer is included as

part of the subcutaneous fat layer. The resulting volume is shown in Figure 3.6.

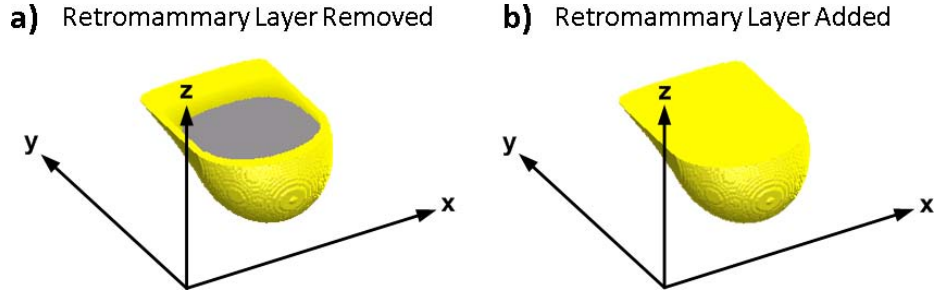


Figure 3.6: Volumes showing the subcutaneous fat layer (yellow) and the fibroglandular region (gray). The retromammary layer is removed in (a) for visualization of the fibroglandular region. The retromammary fat layer is incorporated into the subcutaneous fat layer definition, thus the volume in (b) appears entirely yellow.

3.1.2 Secondary Objects

Secondary objects of the breast are the next level of anatomical detail. These include the subcutaneous-fibrous surface, intraglandular fat, and Cooper's ligaments.

Subcutaneous-Fibrous Surface

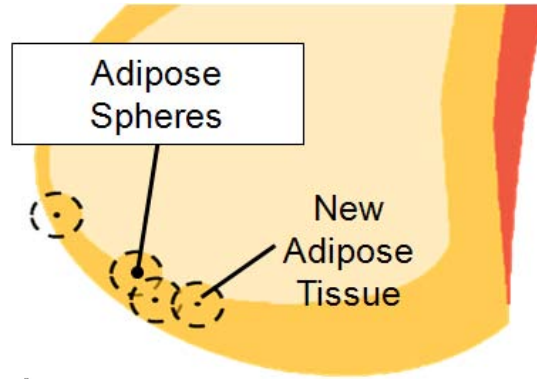


Figure 3.7: 2D Illustration of how spheres are placed to simulate the subcutaneous-fibrous surface

The subcutaneous-fibrous surface refers to the boundary interface between the subcutaneous fat layer and fibroglandular region. Many different breast imaging modalities have shown that the surface between the subcutaneous and fibrous regions is very irregular. Previous hardware phantoms have simulated this surface by creating a layer of tissue-mimicking spheres of 13 mm diameter or by indenting molds with a 3 cm diameter sphere at random depths and locations [20,21]. Our study incorporates a similar approach where 8 mm diameter adipose spheres are added to the phantom near the subcutaneous-fibrous interface. The adipose sphere centers are placed at random locations

at depths between 0-4 mm below the surface within the subcutaneous fat layer. An illustration of this method is shown in Figure 3.7. Fibrous tissue within the fibroglandular region that is overlapped by a sphere is replaced by adipose tissue, while the subcutaneous fat layer and volume outside of the outer boundary is unchanged. The newly added adipose tissue is incorporated into and considered as part of the subcutaneous fat layer. Figure 3.8 shows several partial phantom simulations that show the subcutaneous-fibrous surface for different numbers of spheres: 250, 500, 750, and 1000. The number of spheres is increased until the surface appears sufficiently irregular. Typically 1000 spheres are used.

Ellipsoid Characteristics

Both intraglandular fat and Cooper’s ligaments are simulated as ellipsoids. Each ellipsoid has several characteristics associated with it as shown in Figure 3.9. The equatorial radii, A and B , and the polar radius, C , define the size of the ellipsoid. The center point, (x_0, y_0, z_0) , defines the location of the ellipsoid. The tilt angles, θ and ϕ , are calculated similarly as polar angles with respect to a shifted axis with origin at the ellipsoid center point. The polar radius of the ellipsoid is aligned along these angles to define the orientation.

The equation for an “un-tilted” ellipsoid is as follows:

$$\frac{(x - x_0)^2}{A^2} + \frac{(y - y_0)^2}{B^2} + \frac{(z - z_0)^2}{C^2} \leq 1 \quad (3.12)$$

where A , B , and C are the equatorial and polar radii, and (x_0, y_0, z_0) is the ellipsoid center point.

Intraglandular Fat

In addition to subcutaneous fat, intraglandular fat exists within the breast and is located within the fibroglandular region. Intraglandular fat typically exists as small adipose compartments. In ultrasound studies, it has been shown that intraglandular fat within a breast typically exists as an elongated streak within a B-mode image and is often orientated roughly parallel along the overall ductal branching direction. Given this information, adipose compartments are modeled as small elongated ellipsoids of varying sizes with equatorial radii A and B selected randomly between 1-3 mm, and polar radius C between 4-12 mm. The ratio of $A:C$ and $B:C$ is maintained at 1:4. Their tilt angles, θ and ϕ , are calculated to orient the polar radius along a line connecting the ellipsoid center point and the nipple point. To slightly randomize the orientation, the polar radius is varied from this line by a randomly calculated angle from 0 to 30°. An illustration of adipose

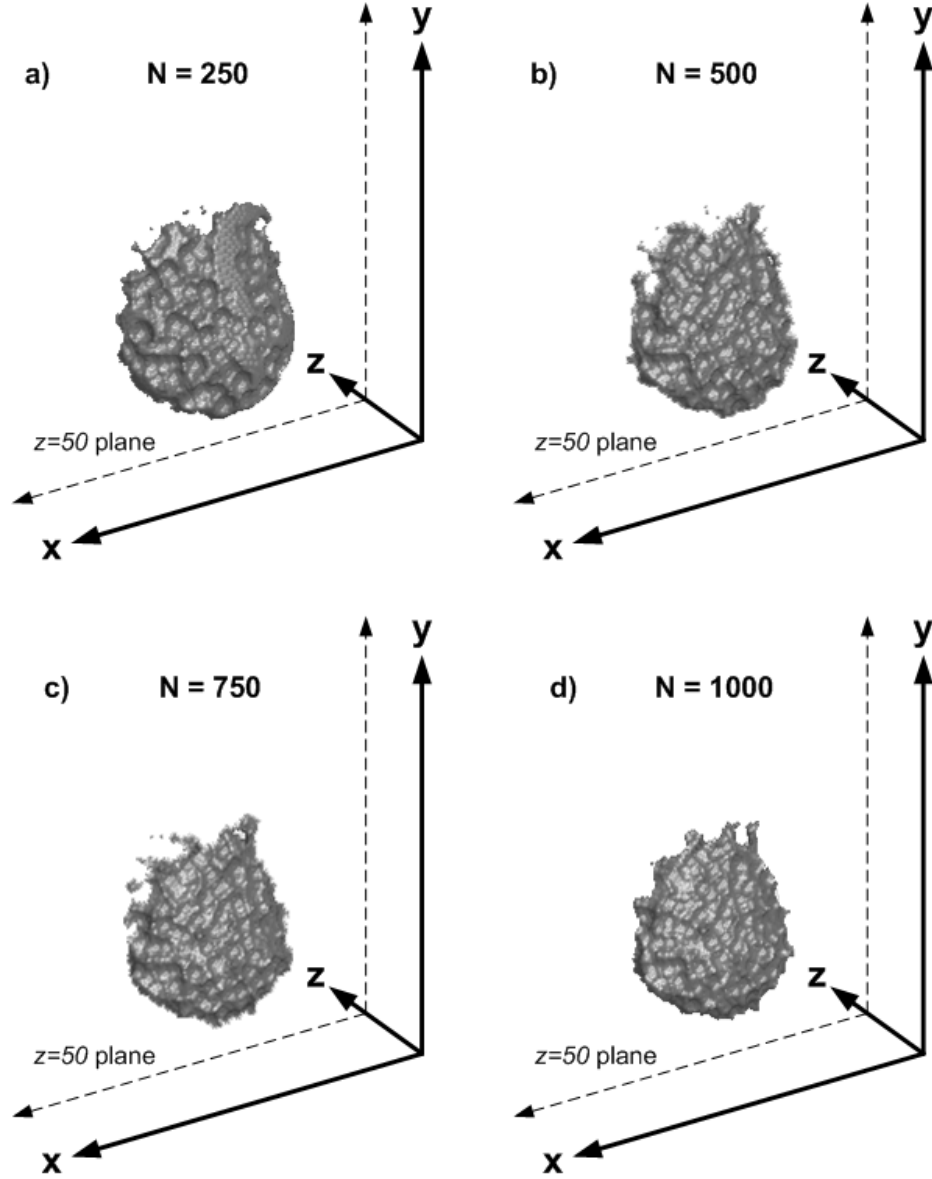


Figure 3.8: Subcutaneous-fibrous surface simulated for different number of spheres. Spheres are added until the surface appears sufficiently irregular. Typically 1000 spheres are added.

compartment orientations is shown in Figure 3.10. The center points are selected randomly within the fibroglandular region. Fibrous tissue overlapped by the ellipsoid is replaced by adipose tissue, while the subcutaneous fat layer and volume outside of the outer boundary is left unchanged.

Both subcutaneous fat and intraglandular fat contribute to the total adipose percentage which is calculated as $[Subcutaneous\ Fat\ Volume + Intraglandular\ Fat\ Volume] / [Total\ Breast\ Volume]$. While adipose percentage content depends on the BMI of the individual, studies have shown that adipose percentage within the breast increases with both age and breast size. In a study by Lee et

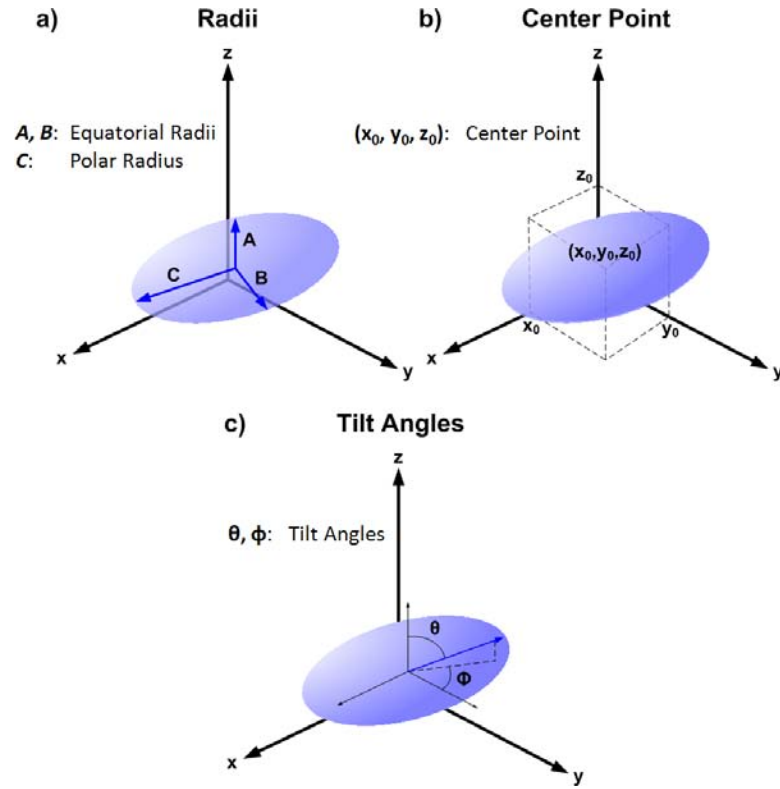


Figure 3.9: Illustration of ellipsoidal characteristics involved for simulation of intraglandular fat and Cooper's ligaments. (a) The equatorial radii and polar radius define the size of the ellipsoid. (b) The center point defines the location of the ellipsoid. (c) The tilt angles define the orientation of the ellipsoid.

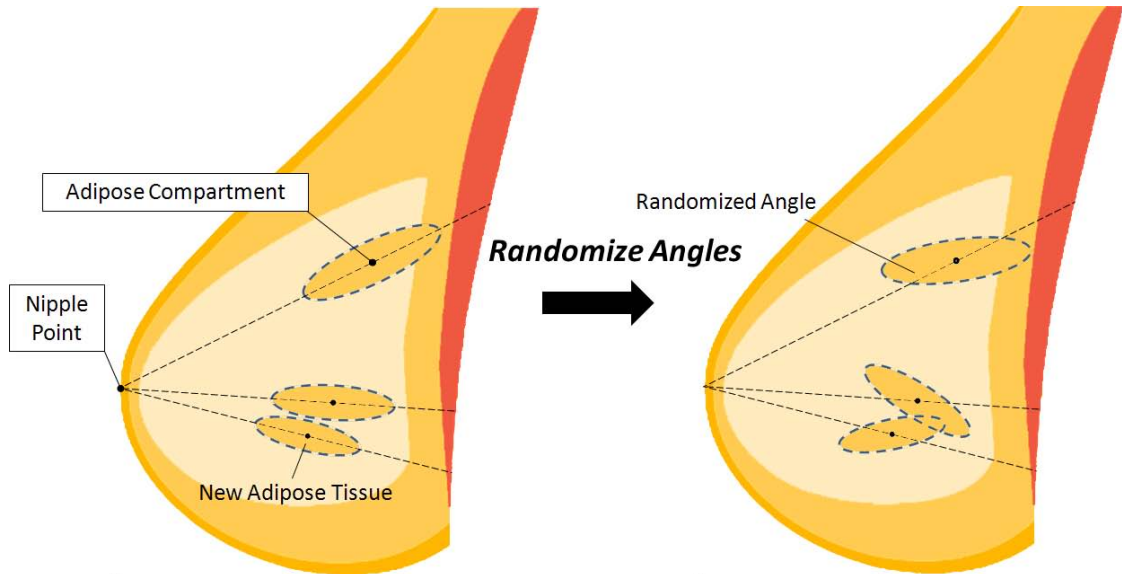


Figure 3.10: 2D illustration showing orientation of adipose compartments. The left side shows the adipose compartments placed with the polar radii aligned with the nipple. The right side shows the adipose compartments after angles are randomized by 0 to 30°.

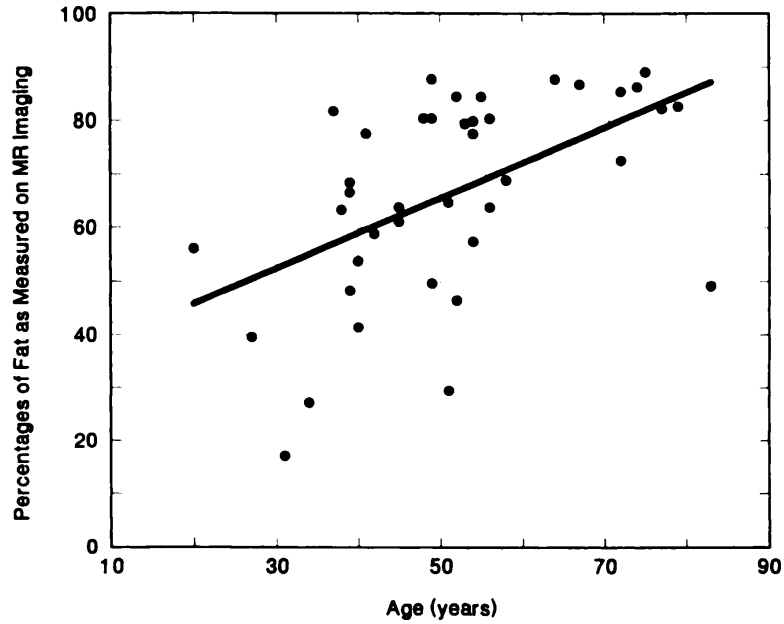


Figure 3.11: Scatter plot diagram shows breast adipose percentage (as measured by MR imaging) vs. patient age [17].

al, a positive correlation between the breast adipose percentage and age of the individual is shown through experimental results. A scatter plot of these results is shown in Figure 3.11 [17].

To determine the number of adipose compartments to produce within a breast, a desired adipose percentage is used. Given a desired adipose percentage for the breast phantom, adipose compartments are added to satisfy this percentage. To further explain, the initial adipose percentage is calculated as the subcutaneous fat volume divided by the total breast volume. Adipose compartments are then added until the desired adipose percentage is reached or exceeded. A flow chart describing this method is shown in Figure 3.12.

The examples in Figure 3.13 show the volumes of four partial phantoms generated with different adipose percentages. By varying adipose percentage, one can attempt to simulate a phantom to model subjects of different BMI and age.

Cooper's Ligaments

Cooper's ligaments are fibrous ligaments that are interwoven within the subcutaneous fat layer and function to connect the fibroglandular region to the skin and pectoral muscle. In images, they tend to appear as thin fibrous compartments that surround adipose tissue. In previous breast phantom studies, Cooper's ligaments have been modeled as thin spherical or ellipsoidal shells located within the subcutaneous fat layer where the shell thickness is designated as fibrous tissue and the inner

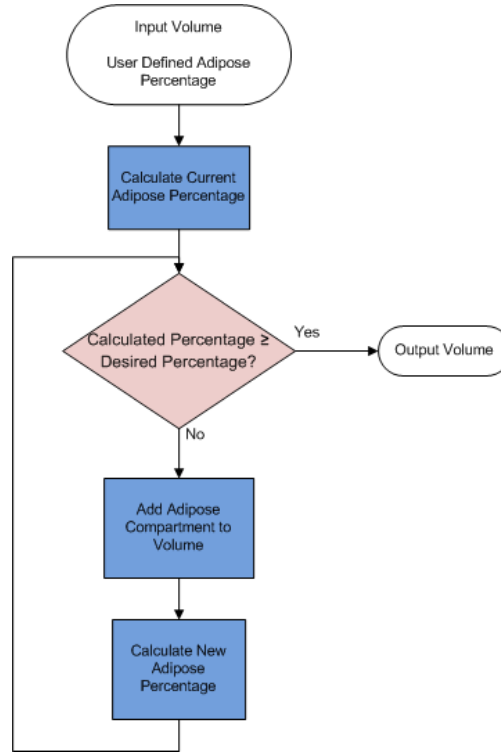


Figure 3.12: Flow chart demonstrating the method for adding adipose compartments to the phantom. Adipose compartments are added until the newly calculated adipose percentage is equal to or greater than the desired adipose percentage.

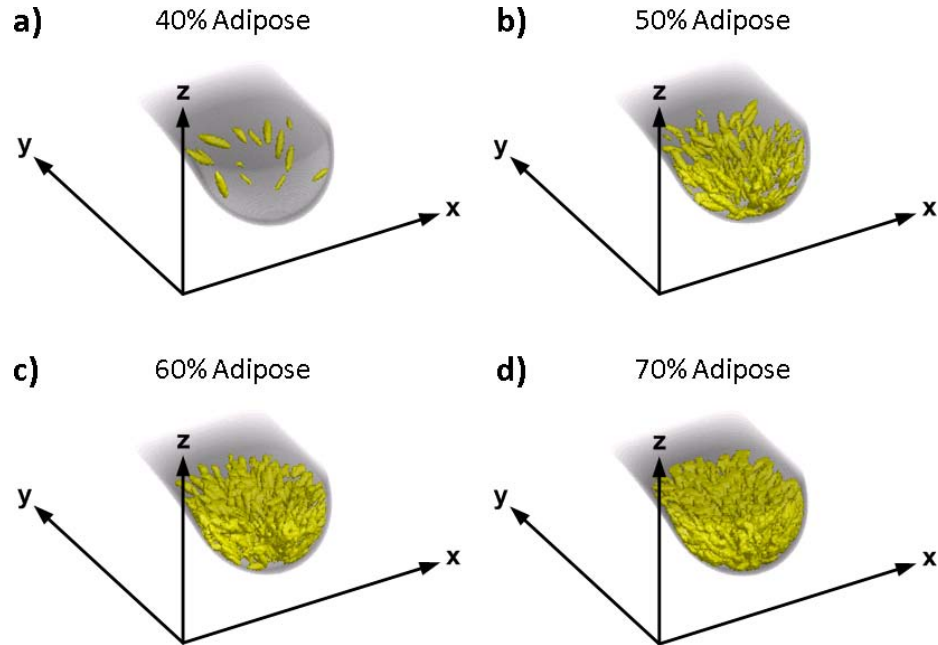


Figure 3.13: Four simulated volumes with different adipose percentages. Adipose compartments are simulated as elongated ellipsoids located within the fibroglandular region that extend towards the nipple at slightly deviated angles.

volume as adipose tissue [1,5]. In our study, Cooper’s ligaments are modeled as elongated ellipsoid shells of varying sizes that exist within the subcutaneous fat layer. The equatorial radii, A and B , are each calculated to be between 6-13 mm and the polar radius, C , is calculated to be 40 mm. The thickness of each shell is approximately 2 mm. The ellipsoidal shell center points are randomly distributed on the outer boundary surface and maintain greater than 26 mm distance between each center to avoid overlapping. Their tilt angles, θ and ϕ , are calculated to orient the polar radius along a line extending from the ellipsoid center point to a central point within the breast ($x = 100$ mm, $y = 50$ mm, $z = 30$ mm). This orientation is chosen so that each shell extends towards and terminates at the subcutaneous-fibrous surface for all ellipsoidal shell locations. An illustration of the Cooper’s ligaments orientation is shown in Figure 3.14. The ellipsoid thickness is designated as fibrous tissue and replaces the adipose tissue within the subcutaneous fat layer that it overlaps. Volumes within the fibroglandular region and outside of outer boundary remain unchanged.

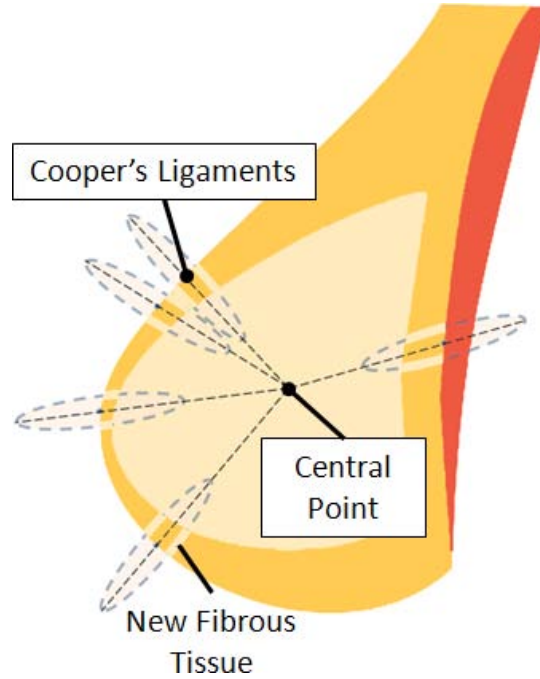


Figure 3.14: 2D illustration showing orientation of Cooper’s ligaments.

The equation modeling an “un-tilted” elongated ellipsoid shell is similar to Equation 3.12, however an additional inequality is used to produce a thickness of 2 mm and is as follows:

$$0.8 \leq \frac{(x - x_0)^2}{A^2} + \frac{(y - y_0)^2}{B^2} + \frac{(z - z_0)^2}{C^2} \leq 1 \quad (3.13)$$

The partial phantom in Figure 3.15 shows Cooper’s ligaments generated within the subcutaneous

fat layer. It is important to note that the Cooper's ligament fibrous tissue only replaces adipose tissue in the subcutaneous fat layer, including tissue added by the subcutaneous-fibrous surface. However, it does not replace intraglandular fat within the fibroglandular region.

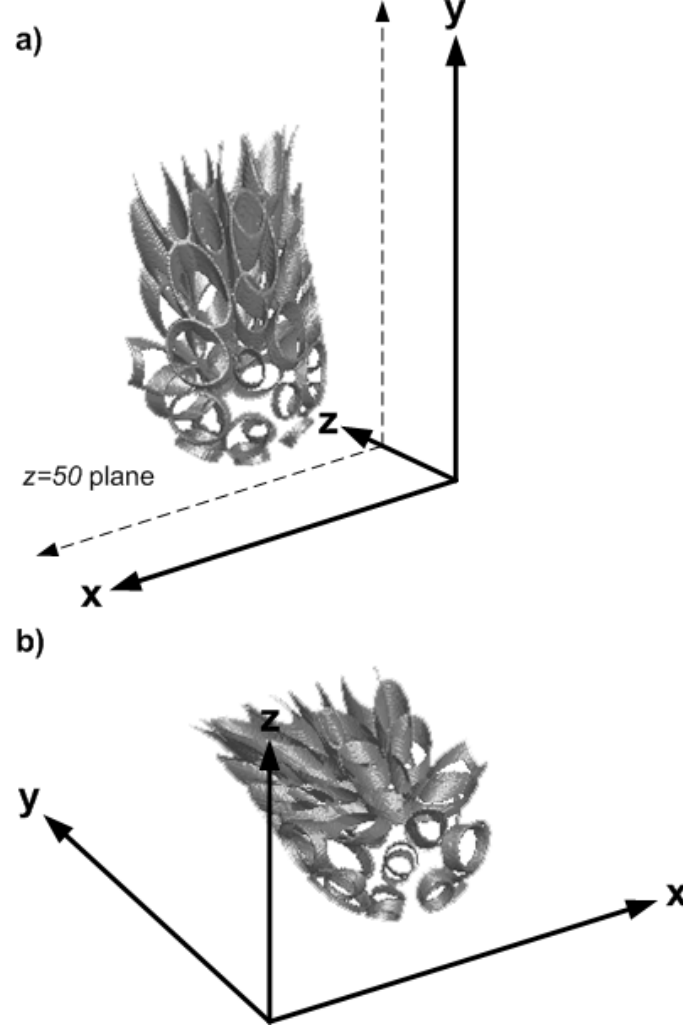


Figure 3.15: Volume showing fibrous tissue of Cooper's ligaments within the subcutaneous fat layer. Cooper's ligaments are simulated as ellipsoidal shells with center points located on the outer boundary that extend towards the center of the breast.

3.1.3 Ductal Structure

There are typically 15-25 ductal lobes in the breast. Each lobe is essentially a ductal tree that is intertwined with other lobes, like roots of a tree [11–14, 19, 24, 26, 27]. Each ductal tree is simulated as a nodal network with associated physical characteristics. The proceeding describes the methods of constructing the nodal network and physical characteristics of the ductal structure.

Nodal Network

Individual ductal trees are simulated following a random binary tree model which is a common method of simulating organic trees in nature [4]. Ramification matrices are a metric used to describe the branching of random binary trees, in which the branching probabilities at specific branches are determined by elements within the matrix. Modeling ductal trees using ramification matrices was originally proposed by Bakic et al, where the ramification matrices were calculated from traced galactograms [3,4].

Random binary trees can be described by a nodal network where each branch is represented as a node. In a random binary tree, the nodal network begins at a single *root node*. Every node, including the root node, branches or “bifurcates” into two other nodes. Thus, each node is a *parent node* and has two *children nodes*. The exception to this is a *terminal node* which does not branch. Each node also has an associated *node order* and *biorder*. The node order is a particular value which is indicative of level or height of the node in the nodal network, with a high number being closer to the root and a low number being closer to the terminal branches. The biorder of a node is the two node orders of the associated children nodes. For instance, if a node has two children nodes of orders 3 and 2, the parent node would be said to have biorder(3,2). Terminal nodes do not have children nodes, thus they do not have a biorder.

Node orders are determined in the following fashion. Terminal nodes have node order equal to 1. The root node has the highest node order, s , and is the start of the nodal network. As previously stated, each node (except terminal nodes) is a parent node and has two children nodes. Given children node orders of i and j , the following can be said of the parent node order k that

$$k = \begin{cases} \max(i, j) & \text{if } i \neq j \\ i + 1 = j + 1 & \text{if } i = j \end{cases} \quad (3.14)$$

Furthermore, a parent of node order k is said to have biorder(i,j) where $i \geq j$. For example, a branch with node order 3 can have biorder(3,1), biorder(3,2) and biorder(2,2) according to the restrictions in Equation 3.14.

Two examples of binary trees with labeled node orders, one simple and one more complex, are shown in Figure 3.16. To label a tree, first, terminal nodes are labeled with node order 1. The parent node orders of the terminal nodes can be found using Equation 3.14, followed by the next parent set, and so on until the entire tree has been filled out.

The ramification matrix is a statistical matrix that describes the binary tree. Each element, r_{ij} ,

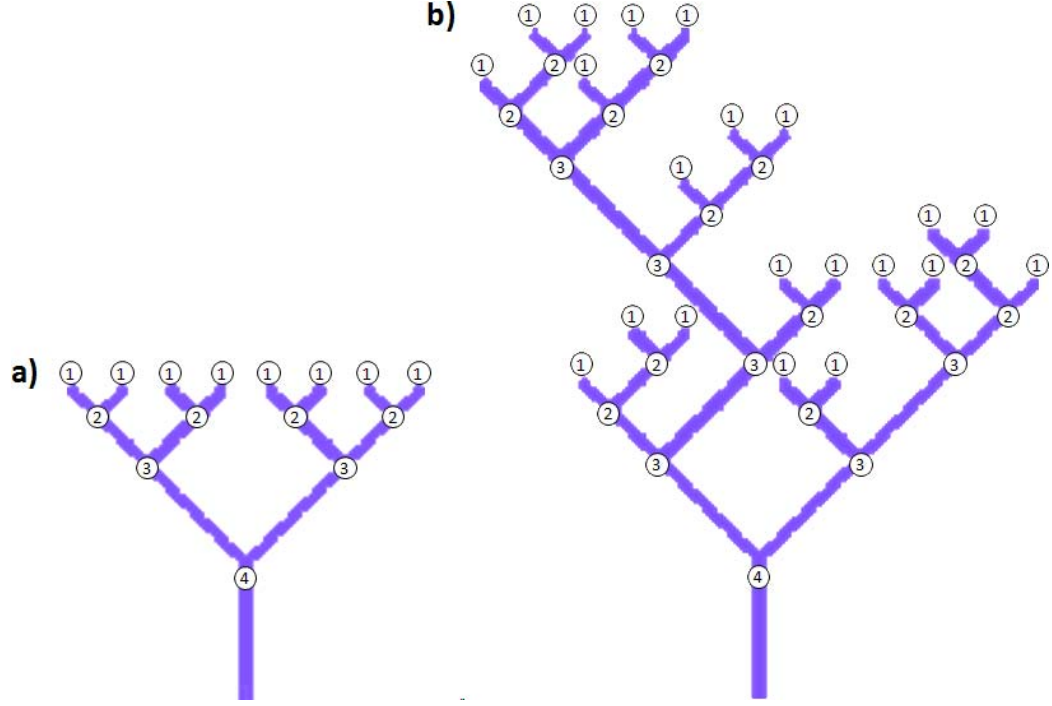


Figure 3.16: Two random binary trees with labeled nodes. Both have different ramification matrices associated with them, as seen in Equation 3.18.

is the probability of a branch with node order k to have biorder(i,j) where $i \geq j$ (Reminder: The value of k in relation to i and j of element r_{ij} is defined in Equation 3.14). The general format of the ramification matrix is

$$R(s) = \begin{bmatrix} r_{2,1}r_{1,1} & 0 & \cdots & 0 & 0 \\ r_{3,1}r_{3,2}r_{2,2} & 0 & \cdots & 0 & 0 \\ \vdots & & & & \vdots \\ \vdots & & & & 0 \\ r_{s,1}r_{s,2} & \cdots & r_{s,s-1}r_{s-1,s-1} & & \end{bmatrix} \begin{array}{l} \leftarrow \text{Node Order 2} \\ \leftarrow \text{Node Order 3} \\ \\ \leftarrow \text{Node Order } s \end{array} \quad (3.15)$$

where s is the root or maximum node order. As an example, a ramification matrix of $s = 4$ is

$$R(s = 4) = \begin{bmatrix} r_{2,1} & r_{1,1} & 0 & 0 \\ r_{3,1} & r_{3,2} & r_{2,2} & 0 \\ r_{4,1} & r_{4,2} & r_{4,3} & r_{3,3} \end{bmatrix} \begin{array}{l} \leftarrow \text{Node Order 2} \\ \leftarrow \text{Node Order 3} \\ \leftarrow \text{Node Order 4} \end{array} \quad (3.16)$$

As stated earlier, the elements r_{ij} represent the biorder probabilities for node order k . Each row represents the probabilities of all possible biorders for a given node order k ranging from 2 to s as illustrated in Equations 3.15 and 3.16. Therefore the sum of each row is equal to 1 or 100%. Node order 1 does not have biorder probabilities because they are terminal branches.

To generate the ramification matrix from a given tree, one can first label the nodes of a tree as shown in Figure 3.16. Each element r_{ij} can then be calculated the following way:

$$r_{ij} = \frac{b_{ij}}{a_k} \quad (3.17)$$

where a_k is the number of nodes of order k , and b_{ij} is equal to the number of nodes with biorder(i,j). For instance, to find the element $r_{2,2}$ for the tree in Figure 3.16b, we first find a_3 because the associated node order of $r_{2,2}$ is $k = 3$. The total number of nodes having node order 3 is 6, therefore we have $a_3 = 6$. Next, to find $b_{2,2}$, we find the total number of nodes with biorder(2,2). There are 2 nodes that have biorder(2,2) (Note: The nodes that have biorder(2,2) will always have node order 3 due to Equation 3.14). Now we can simply calculate $r_{2,2}$ to be $2/6 \approx 0.33$. This element is then placed in the ramification matrix into the appropriate position. As an example, the ramification matrices for both the trees shown in Figure 3.16 are

$$R_a(s = 4) = \begin{bmatrix} 0 & 1.0 & 0 & 0 \\ 0 & 0 & 1.0 & 0 \\ 0 & 0 & 0 & 1.0 \end{bmatrix} \text{ and } R_b(s = 4) = \begin{bmatrix} 0.385 & 0.615 & 0 & 0 \\ 0 & 0.67 & 0.33 & 0 \\ 0 & 0 & 0 & 1.0 \end{bmatrix} \quad (3.18)$$

To generate a random binary tree from a ramification matrix, one can use the probability elements in the ramification matrix to calculate the biorder of the root node and generate a new pair of nodes. The biorder of these new nodes can be calculated using the ramification matrix elements as well, and so on, until terminal nodes are reached. Figure 3.17 presents an example of this procedure using the ramification matrix R_b from Equation 3.18.

In the experiment performed by Bakic et al, galactograms were traced and a ramification matrix to model the resulting ductal trees was generated [3, 4]. The resulting matrix after rounding to the nearest hundredth is

$$R(s = 4) = \begin{bmatrix} 0.36 & 0.64 & 0 & 0 \\ 0.35 & 0.29 & 0.36 & 0 \\ 0.29 & 0.28 & 0.23 & 0.20 \end{bmatrix} \quad (3.19)$$

An example of a ductal tree generated using this ramification matrix yields the volume shown in Figure 3.18a. Speculation leads us to believe that the ductal tree may branch a few more node orders. We believe this due to the nature of galactograms in that it is very difficult to differentiate branches as they get closer to lobules, thus the tracings may not have been able to include these

Start with the root of node order 4.

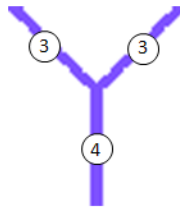
For node order 4, there is 100% probability of the root node having $\text{biorder}(3,3)$.



Add two child branches with node order 3.



For node order 3, the probability of having $\text{biorder}(3,1)$, $\text{biorder}(3,2)$, and $\text{biorder}(2,2)$ are 0%, 67%, and 33% respectively.



Use a random number generator to determine the result. Here, the result is $\text{biorder}(3,2)$



Add two child branches, one with node order 3 and the other with node order 2.

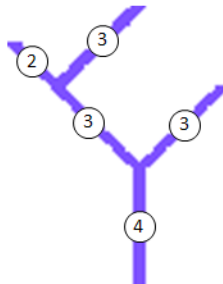


Figure 3.17: Example of procedure to generate a random binary tree from a ramification matrix. The ramification matrix used in this example is R_b from Equation 3.18.

smaller branches. For this reason, we generate ductal trees using the following ramification matrix.

$$R(s=6) = \begin{bmatrix} 0 & 1.0 & 0 & 0 & 0 & 0 \\ 0 & 0 & 1.0 & 0 & 0 & 0 \\ 0 & 0 & 0.36 & 0.64 & 0 & 0 \\ 0 & 0 & 0.35 & 0.29 & 0.36 & 0 \\ 0 & 0 & 0.29 & 0.28 & 0.23 & 0.20 \end{bmatrix} \quad (3.20)$$

This causes the binary tree to branch with the parameters in Equation 3.19 but to have an additional two degrees of branching when normally the tree would terminate. An example of a ductal tree generated using the ramification matrix in Equation 3.20 is shown in Figure 3.18b.

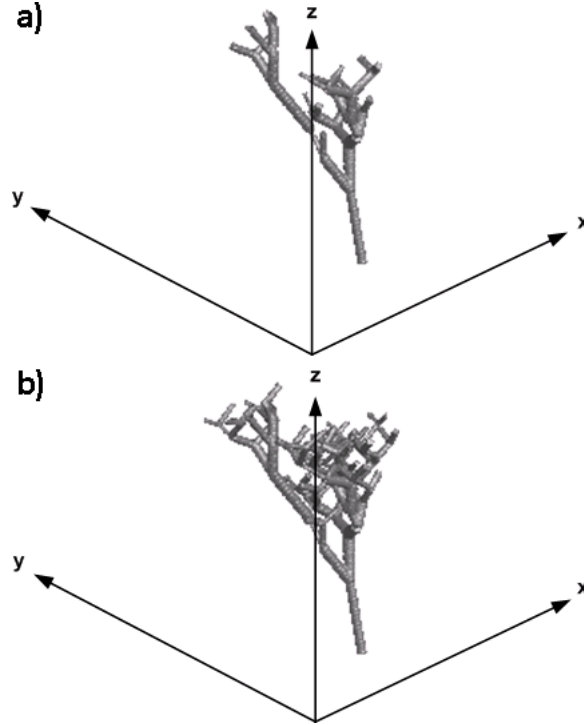


Figure 3.18: The above examples show two ductal trees generated from two different ramification matrices. (a) The first ductal tree was generated using the ramification matrix in Equation 3.19. (b) The second ductal tree generated using the ramification matrix in Equation 3.20. Notice that the second ductal tree has additional degrees of branching due to the larger ramification matrix in Equation 3.20.

Physical Characteristics

Besides the connectivity of the nodal network, each branch has physical characteristics associated with it. The physical characteristics of individual branches are demonstrated in Figure 3.19a-c.

Each branch is represented as a cylinder which has height and radius, and starting and ending points (Figure 3.19a). Each also has two sets of angles associated with them. The first pair are the lobe angles, α and β , and define the *lobe axis* which is an axis specific to each lobe/tree and defined the overall direction of the ductal tree (Figure 3.19b). Every branch in the same ductal tree has the same α , β , and lobe axis. Branch angles, θ and ϕ , are angles with respect to the lobe axis and define the direction of each branch (Figure 3.19c).

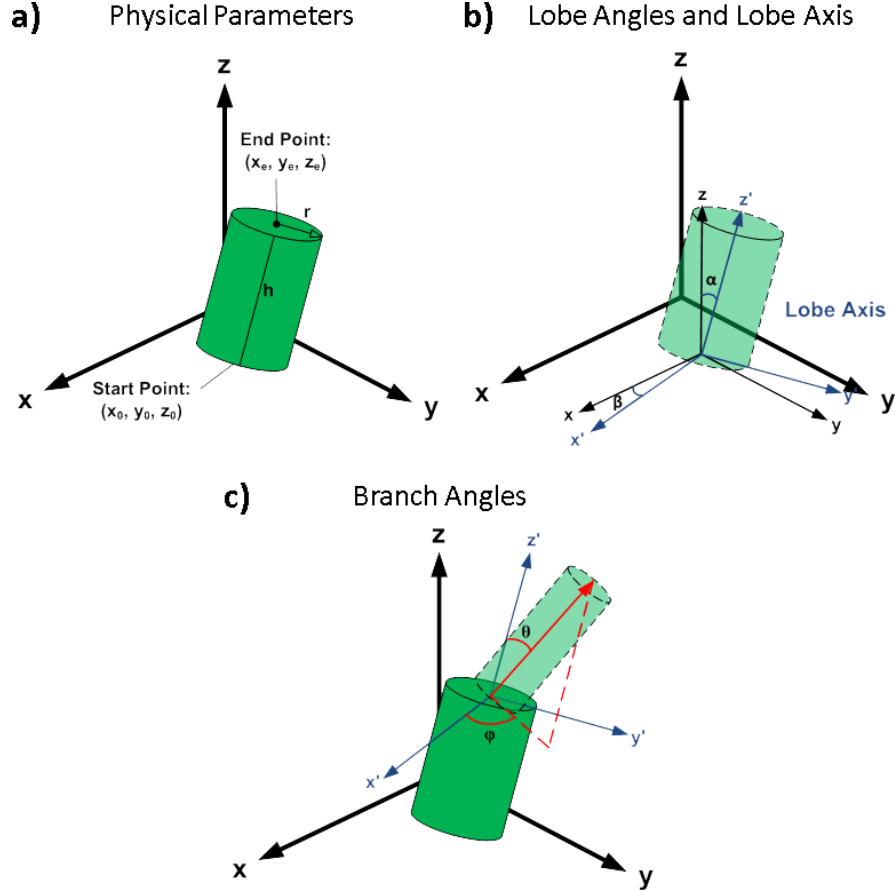


Figure 3.19: Illustration of physical characteristics of ducts. (a) Physical parameters include radius, height, and spatial locations of start and end points of each branch. (b) Lobe angles define the “Lobe Axis” by rotating a shifted axis by α and β . The lobe axis is unique to each ductal tree. (c) Branch angles define the branching angle and are calculated with respect to the lobe axis.

The height, h , and radius, r , of each branch decrease with increasing node order k and are calculated as:

$$h = h_0 \frac{k}{s} \text{ where } h_0 = 8 \text{ to } 12 \text{ mm} \quad (3.21)$$

$$r = r_0 \frac{k}{s} \text{ where } r_0 = 1 \text{ to } 2 \text{ mm} \quad (3.22)$$

where s is the value of the root node (equal to 6 for our case), and h_0 and r_0 are calculated as

random lengths between 8-12 mm and 1-1.2 mm respectfully. The values of h_0 and r_0 are calculated to agree with the size of early ductal branches taken from anatomical studies [13, 24, 26]. Both h_0 and r_0 are recalculated each time a branch is created to produce height variability for each branch. This is necessary because if the same node orders all have the same branch height, the regularity of the tree appears too “crystalline” in nature, rather than “natural”. This is evident in Figure 3.20, where the tree in Figure 3.20a has constant branch height and radius for each node and the tree in Figure 3.20b has variable branch height and radius. The tree in Figure 3.20b appears much more natural. This method of calculation in Equations 3.21-3.22 produces height variability, while maintaining a relatively constant height:radius ratio for each branch.

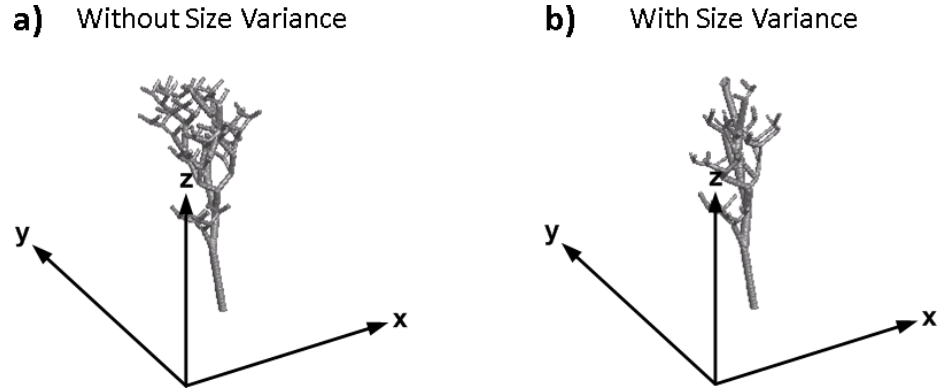


Figure 3.20: (a) The first ductal tree was generated without height and radius variance for each node order with h_0 and r_0 equal to 10 mm and 1.5 mm respectively. (b) The second ductal was generated with height and radius variance for each node order with h_0 and r_0 equal to 8 to 12 mm and 1 to 2 mm respectively.

The *lobe axis* associated with each tree is unique for that ductal tree. The lobe axis is an axis with origin located at the base of the ductal tree. It is used to determine the overall branching direction of the tree. α and β rotate the original axis (x -, y -, and z -axis) that has been shifted to the base of the tree to form the new lobe axis (x' -, y' -, and z' -axis). β is the angle that rotates the x -axis and y -axis around the z -axis and α is the angle that rotates the z -axis around the y -axis. The rotation and the resulting lobe axis for example ductal trees are shown in Figure 3.21. By mapping the ductal trees on a specific lobe axis, the entire ductal tree can be oriented along a given direction.

When generating new branches, a reference lobe axis is set with origin located at the endpoint of the parent branch (or starting point of the two children branches) as seen in Figure 3.22. Children branches are generated in pairs that exist within a unique plane that contains the reference lobe

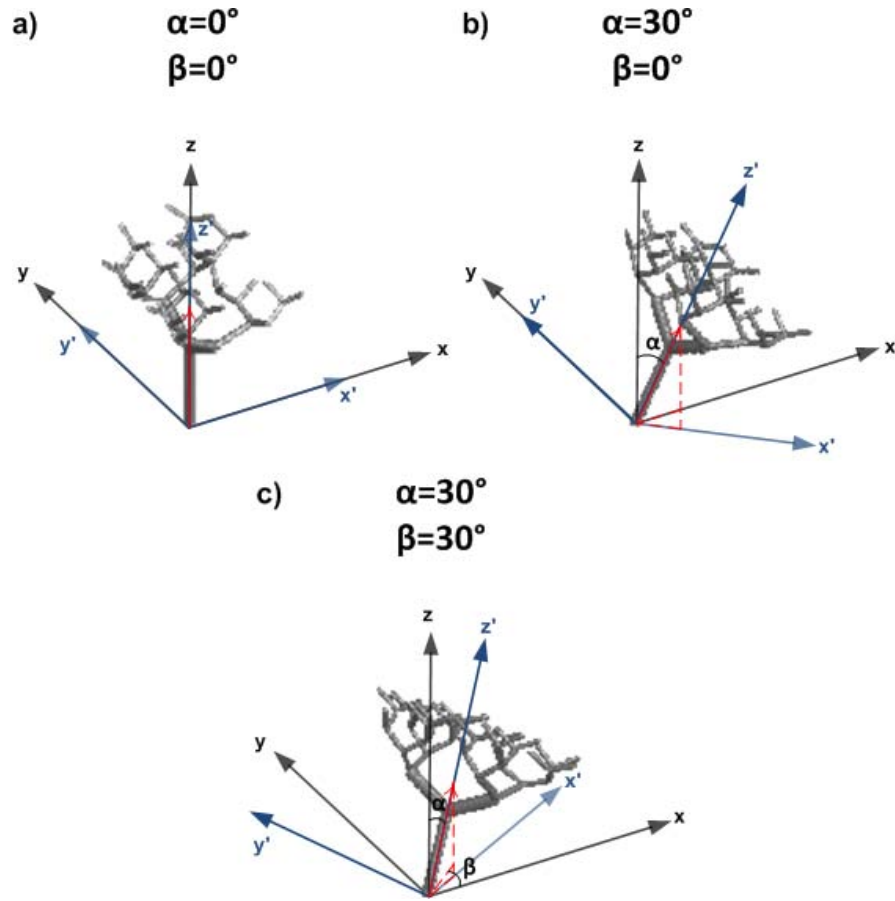


Figure 3.21: Examples of the same ductal tree orientated along different lobe axes at different rotational lobe angles. Notice that tilting the lobe axis along angles α and β tilts the entire ductal tree.

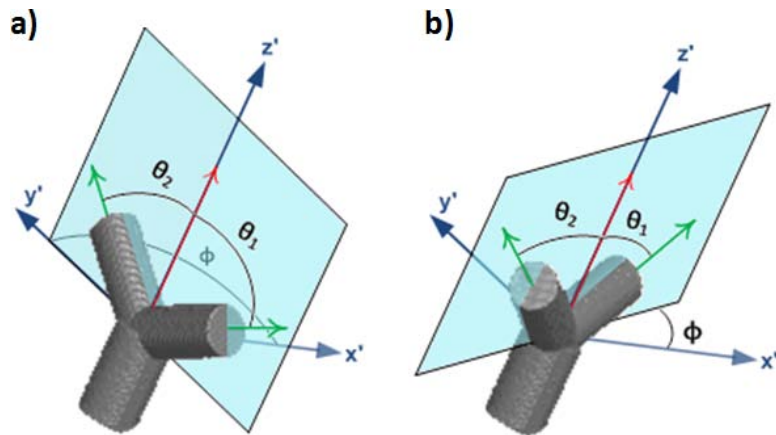


Figure 3.22: Two examples above show orientation of branching angles with respect to the reference lobe axis. Reference lobe axes are defined with origin at the new branching point. Branching angles are calculated with respect to the reference lobe axis. θ_1 and θ_2 are calculated with respect to the z' -axis and ϕ is calculated with respect to the x' -axis.

z' -axis. This plane is rotated by angle ϕ with respect to the reference x' -axis and is calculated as

$$\phi = \phi_p + \phi' + 90^\circ \quad (3.23)$$

where ϕ_p is the previous rotated angle associated with the parent node and ϕ' is a random angle between -15° and 15° . Within this plane, the two children branches are at angles θ_1 and θ_2 with respect to the reference lobe z' -axis. When the child branch node orders i and j are equal to each other, θ_1 and θ_2 are calculated as

$$\theta_1 = 60^\circ + \theta' \quad , \quad \theta_2 = -60^\circ + \theta' \quad \text{when } i = j, \quad (3.24)$$

where θ' is a random angle between -10° and 10° . When child branch node orders i and j are not equal, we have

$$\theta_1 = (30^\circ + \theta') \frac{j}{i-1} \quad , \quad \theta_2 = (-30^\circ + \theta') \frac{i-j}{i-1} \quad \text{when } i \neq j, \quad (3.25)$$

where ($i \geq j$). A visualization of the branching angles ϕ , θ_1 , and θ_2 is illustrated in Figure 3.22.

The calculations in Equations 3.21-3.25 are adapted from the software phantom study by Bakic et al [3].

Initiation

The starting branches of the ductal trees are positioned based on anatomical data of ductal openings [25]. Twenty-one ductal tree starting points are predefined within 3 mm radius of the nipple point. Depending on the number of ductal trees to be generated in the phantom, the starting points for each tree are selected from this pool of predefined points. The lobe angles of each ductal tree are also predefined based on the starting point position. The lobe angles are designed to ensure each tree branches radially with respect to the nipple point as well as extend into the fibroglandular region with room for the tree to grow laterally [11, 13, 24]. The starting coordinates and associated lobe angles of the starting branches are shown in Table 3.3 and their relative positions to each other are shown in Figure 3.23. All twenty-one starting branches for each ductal tree are displayed in Figure 3.24.

Ductal Opening Locations			
Label	Spatial Location (mm)	Lobe Angle β	Lobe Angle α
1	(100,50,0)	90°	10°
2	(103,50,0)	10°	45°
3	(102.6,51.5,0)	30°	45°
4	(101.5,52.6,0)	60°	45°
5	(100,53,0)	90°	45°
6	(98.5,52.6,0)	120°	45°
7	(97.4,51.5,0)	150°	45°
8	(98.5,47.4,0)	170°	45°
9	(97.4,48.5,0)	190°	35°
10	(98.5,47.4,0)	230°	25°
11	(100,47,0)	270°	25°
12	(101.5,47.4,0)	310°	25°
13	(101,51,0)	350°	35°
14	(101.5,50,0)	25°	25°
15	(101,51,0)	60°	25°
16	(100,51.5,0)	90°	25°
17	(99,51,0)	120°	25°
18	(98.5,50,0)	155°	25°
19	(99,49,0)	190°	15°
20	(100,48.5,0)	270°	10°
21	(101,49,0)	250°	15°

Table 3.3: Ductal opening locations and initial branch directions. The spatial locations indicate the starting branch coordinates near the nipple and the lobe angles indicate the direction of the lobe axis for each ductal tree.

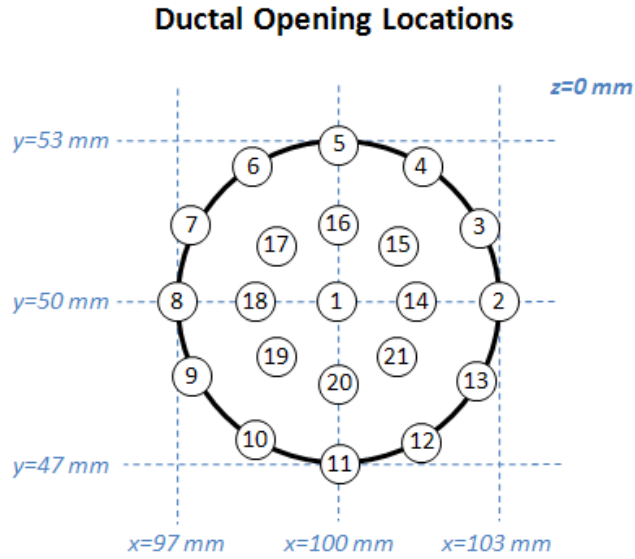


Figure 3.23: Relative locations of each ductal opening

Tissue Placement

The majority of ductal trees exist in the fibroglandular region. However, because ductal trees start at the nipple surface, they must extend through the subcutaneous fat layer before reaching the

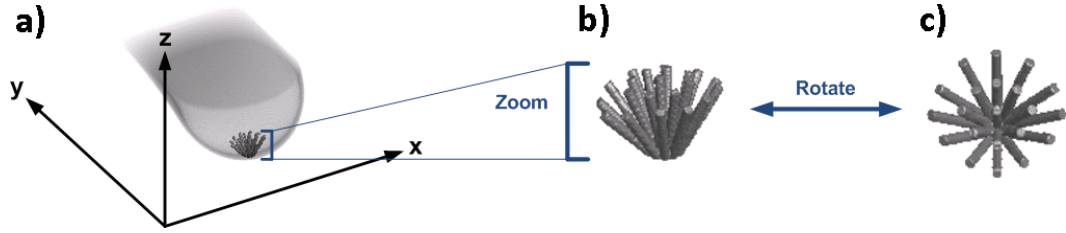


Figure 3.24: Simulation showing locations, distribution and lobe angles of all twenty-one ductal tree starting branches corresponding to ductal openings. The first image (a) shows how the branches extend into the fibroglandular region. The next two images (b-c) show an enlarged version of the starting branches showing their spatial locations, distribution and lobe angles in relation to each other. In actual simulation, only a portion of starting branches is used and the size of each branch varies.

fibroglandular region. Anatomical studies have shown that the ductal radius is approximately 1-2 mm in close proximity to the nipple [19]. Thus, the radius of the duct as it passes through the subcutaneous region is set to be a smaller random radius between 1-2 mm. Once the starting branch has passed through the subcutaneous fat layer, the duct assumes its originally calculated radius from Equation 3.21.

Tissue that is overlapped by cylinders representing each ductal branch is designated as glandular tissue. The cylinders replace all tissue types (adipose and fibrous tissue) in this manner, with the exception being within the subcutaneous fat layer, which replaces tissue at a smaller radius as described. This is illustrated in Figure 3.25.

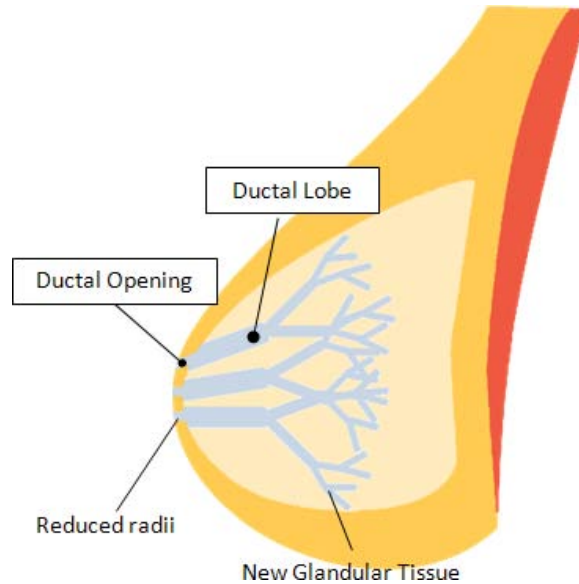


Figure 3.25: 2D illustration showing glandular tissue placement of ductal lobes.

Growth Condition

Each time a pair of children branches is calculated, it is checked that both branches are within the bounds of the fibroglandular region. Additionally, it is checked that they are not overlapping with other existing branches. This is done by comparing each new branch against the radius and spatial locations of each existing branch in the network. If both constraints are satisfied, the branch pairs are accepted and added to the ductal network. If at least one of the constraints is not satisfied, the node orders and physical characteristics of the children branches are recalculated in the same probabilistic manner. If after 30 recalculations the children branches are still not accepted, no branch is generated from the parent node and the parent node is designated as a terminal node by reassigning the parent branch to have node order *1*. In some cases, the reassignment of node order *1* may cause a violation of Equation 3.14, however this violation is ignored.

Ductal Tree Generation

The complete method of generating ductal trees is illustrated in the flowchart in Figure 3.26. Ductal generation begins with between 15 and 21 starting branches which will each generate into a ductal tree. When the starting branches are determined, the characteristics of each starting branch is stored into an array. The generation sequence begins by examining the first starting branch in the array and determining the appropriate characteristics of the children branches for that branch. If the children branches are accepted, they are added to the end of the array. After examination of the first starting branch is complete, the next branch in the array (second starting branch) is examined. This process continues by sequentially examining each branch in the array including new ones that have been added. The end of the process occurs once the end of the array has been reached after examining all branches. This process allows ductal trees to grow simultaneously.

Lobules

Lobules are positioned at the end of terminal ductal branches. As stated in the literature, they are typically made up of 10-100 acini that are approximately 0.15 mm in diameter [19]. The lobules themselves are typically 1-2 mm diameter. Past software breast phantoms have modeled lobules as spheres [1,5]. In our simulation, lobules are modeled as a cluster of three spheres for added texture and irregularity.

Each sphere has a random diameter between 1-2 mm. One sphere is placed at the end point of the terminal branch. Two other spheres are placed at distance 0.5 mm from the terminal branch

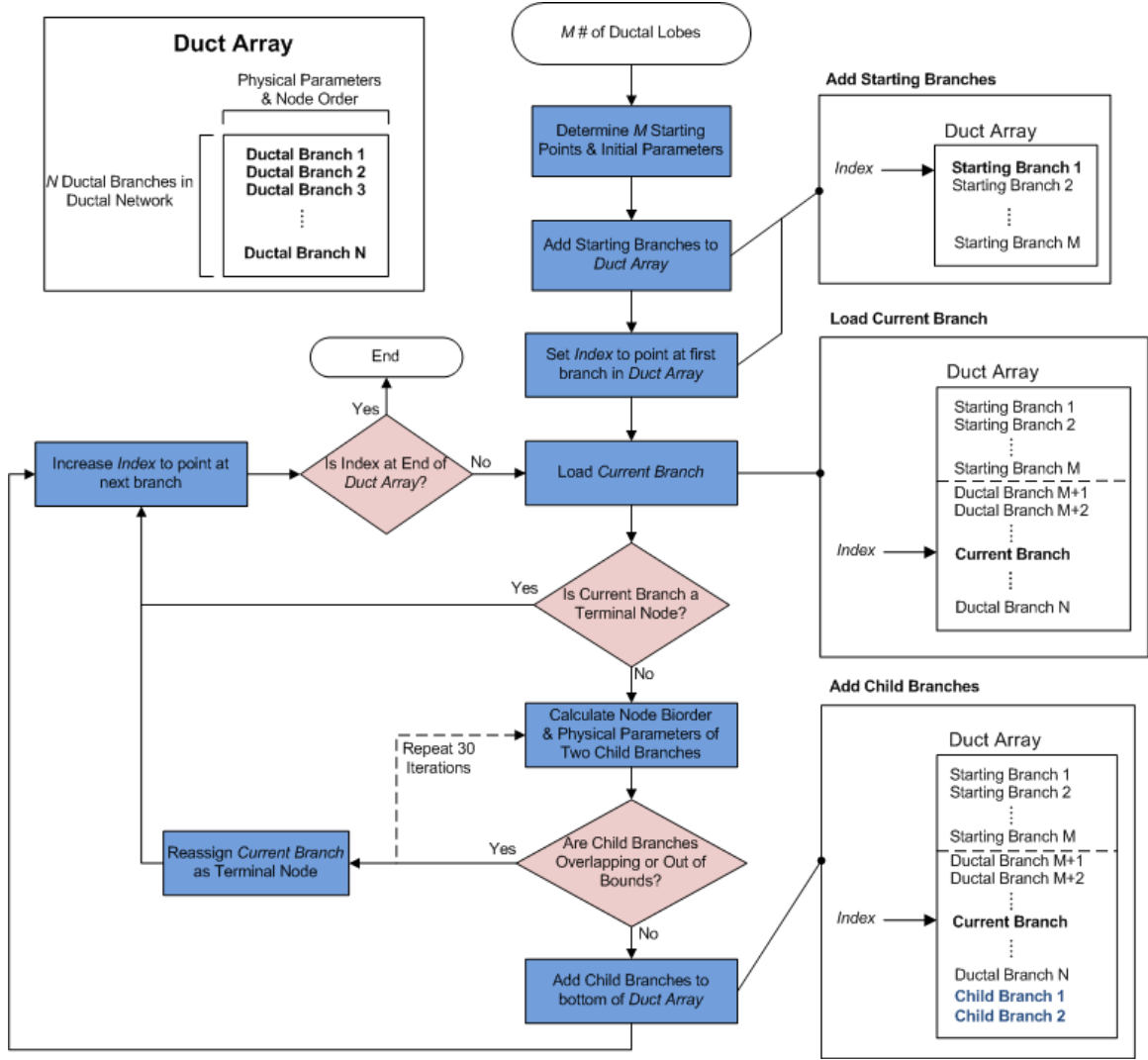


Figure 3.26: Flowchart demonstrating methods of building the ductal structure. The number of ductal trees to be generated is first used to determine the initial starting branches of the array. Children nodes are subsequently generated from these starting branches and form new branches added to the array. The process continues until all branches in the duct array have been examined.

end point at random directions. An illustration of tissue placement for lobules is shown in Figure 3.27. Figure 3.28 shows a simulated ductal tree before and after lobule placement as well as close-up view of the lobule structures.

Complete Ductal Structure

In our simulation, 15 to 21 starting points are selected and ductal trees are generated simultaneously as described to exist primarily in the fibroglandular region. Once all ductal trees are complete, lobules are added. The resulting structure is the complete ductal structure. An example of the

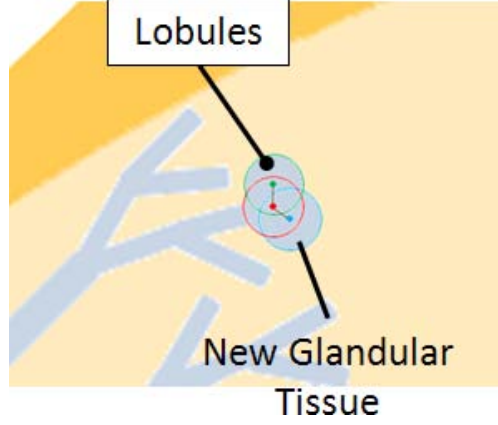


Figure 3.27: Illustration of lobule sphere clusters

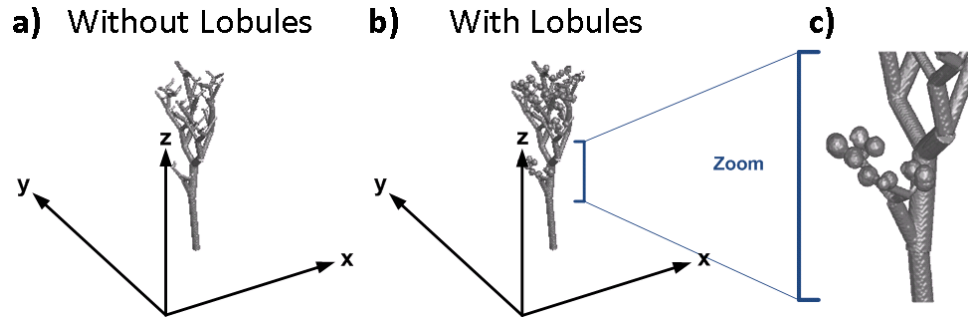


Figure 3.28: (a) The first volume shows a ductal tree without lobules attached to the terminal nodes, (b) while the second shows the same ductal tree with lobules attached. (c) The third volume shows a close-up of the lobule structures.

complete ductal structure generated within a breast volume including fibroglandular region and subcutaneous fat layer is shown in Figure 3.29.

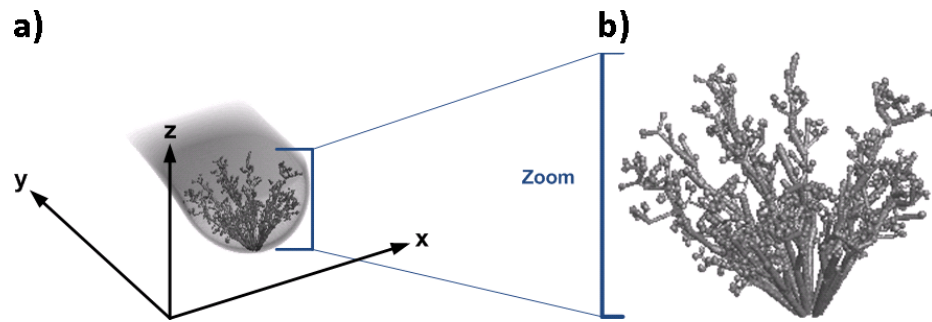


Figure 3.29: Complete ductal structure for 15 ductal trees within a breast volume.

3.1.4 Complete Phantom

The complete phantom is the compilation of all of the subsequent structures: Breast boundary, subcutaneous fat layer, fibroglandular tissue region, subcutaneous-fibrous surface, intraglandular

fat, Cooper's ligaments, and ductal structure. A specific generation sequence is necessary as certain structures build upon others and the corresponding flowchart is shown in Figure 3.30. Each structure process can be thought of containing its own specific generation process.

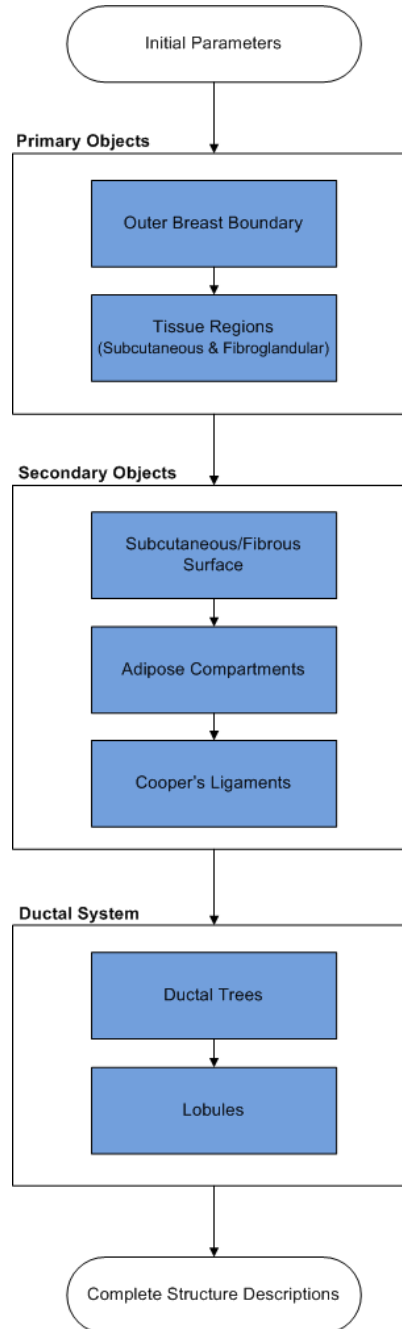


Figure 3.30: Flowchart of phantom generation sequence. The complete phantom is the compilation of all of the structures and a specific generation sequence is necessary as certain structures build on others. Each structure can thought of its own specific generation process. Upon completion, structures are ready for visualization.

3.2 Visualization

Each structure is defined by an array of geometric descriptions defining the size and spatial locations of various geometric objects that compose each structure. Upon completion of the generation sequence, we have geometric descriptions of each structure. For example, we have equations to describe the outer and inner boundaries to define the subcutaneous and fibroglandular tissue regions, an array of sphere locations and radii to describe the subcutaneous-fibrous surface, an array of ellipsoid locations and radii to describe intraglandular fat and Cooper's ligaments, an array of cylinders to describe the ductal trees, and an array of sphere locations and radii to describe lobules. These measurements are continuous (non-discrete) and can be thought of as existing in *object space* with units in millimeters. We can think of object space as being the continuous measurement values of the breast with no dimension or resolution limits as shown in Figure 3.31a. The next step is to *map* these objects in object space to a new coordinate system of a different scale.

The phantom is represented as a discrete three-dimensional voxel matrix called the *phantom matrix* that is said to exist within *phantom space* with dimension units in pixels (Figure 3.31b). The process of taking a volume that exists in object space and then representing it appropriately in phantom space with a different scale or resolution is called *mapping*, where scale and resolution are the same value and their names are used interchangeably. Phantom space can be thought of as a portion of object space with a different scale and shifted axes compared to the axes of object space (Figure 3.31b). This allows the phantom to represent the entire breast or portion of the breast, with variable resolution.

To represent the phantom digitally, the continuous volumes in phantom space must be converted into a discrete matrix called the phantom matrix (Figure 3.31c). Phantom space is continuous, while the phantom matrix represents the discrete coordinate values of phantom space where each element in the matrix is located at discrete coordinates and represents a small volume element of phantom space called a voxel. A voxel is the three-dimensional equivalent of a pixel. The tissue type of each voxel is determined by the locations and properties of the objects in the volume set. The size of the matrix is determined by user defined object space dimensions and resolution. The process of representing a continuous volume object as a discrete three-dimensional matrix is called *discretization*.

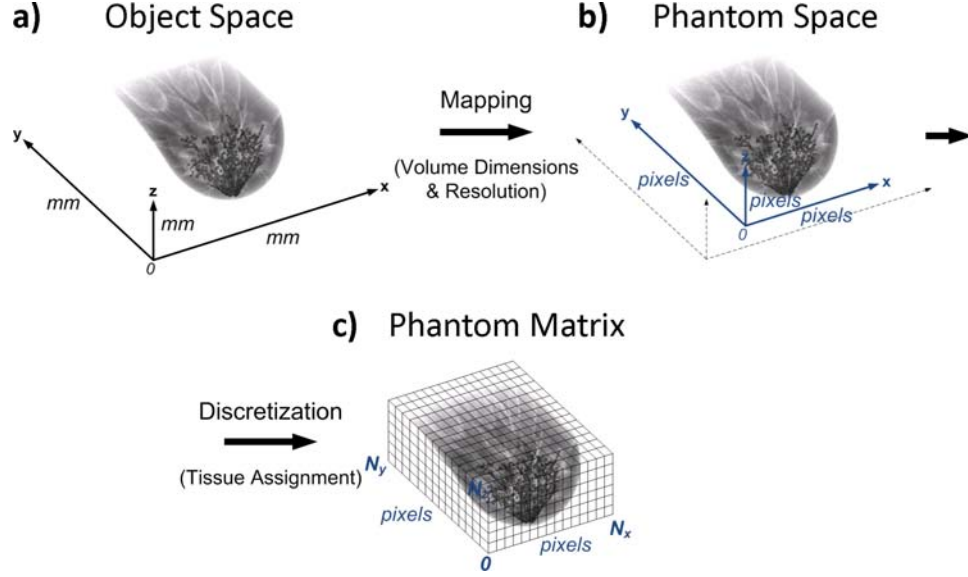


Figure 3.31: The above sequence demonstrates an overview of the visualization process. (a) Given structures described in continuous object space, the structures are mapped into (b) phantom space given user defined volume dimensions and resolution. (c) The structures in phantom space are then represented by the phantom matrix by assigning matrix elements as tissue types based on the properties of these structures.

3.2.1 Mapping Object Space to Phantom Space

To generate the appropriate volume in phantom space, we must map structures from object space into phantom space using a mapping equation. To generate this mapping equation, the mapping parameters are first defined.

The dimensions of object space that are mapped or represented in phantom space are user defined where the maximum volume that can be represented is 200 x 200 x 50 mm in the x -, y -, and z -directions respectfully. The dimension limits are user defined in object space and have units in millimeters. They are shown in Figure 3.32b and are x_{lower} , x_{upper} , y_{lower} , y_{upper} , z_{lower} , and z_{upper} . The resolution is a user defined value that defines the conversion between object space units (millimeters) to phantom space units (pixels) and has units pixels/mm. The resolution value is defined as the variable Res and is equal for all directions, x -, y -, and z - (Figure 3.32b-c).

The mapping equation calculates the equivalent phantom space coordinates from object space coordinates and can be defined as

$$\begin{aligned}
 x_{\text{ph}} &= (x_{\text{obj}} - x_{\text{lower}}) \cdot Res \\
 y_{\text{ph}} &= (y_{\text{obj}} - y_{\text{lower}}) \cdot Res \\
 z_{\text{ph}} &= (z_{\text{obj}} - z_{\text{lower}}) \cdot Res
 \end{aligned} \tag{3.26}$$

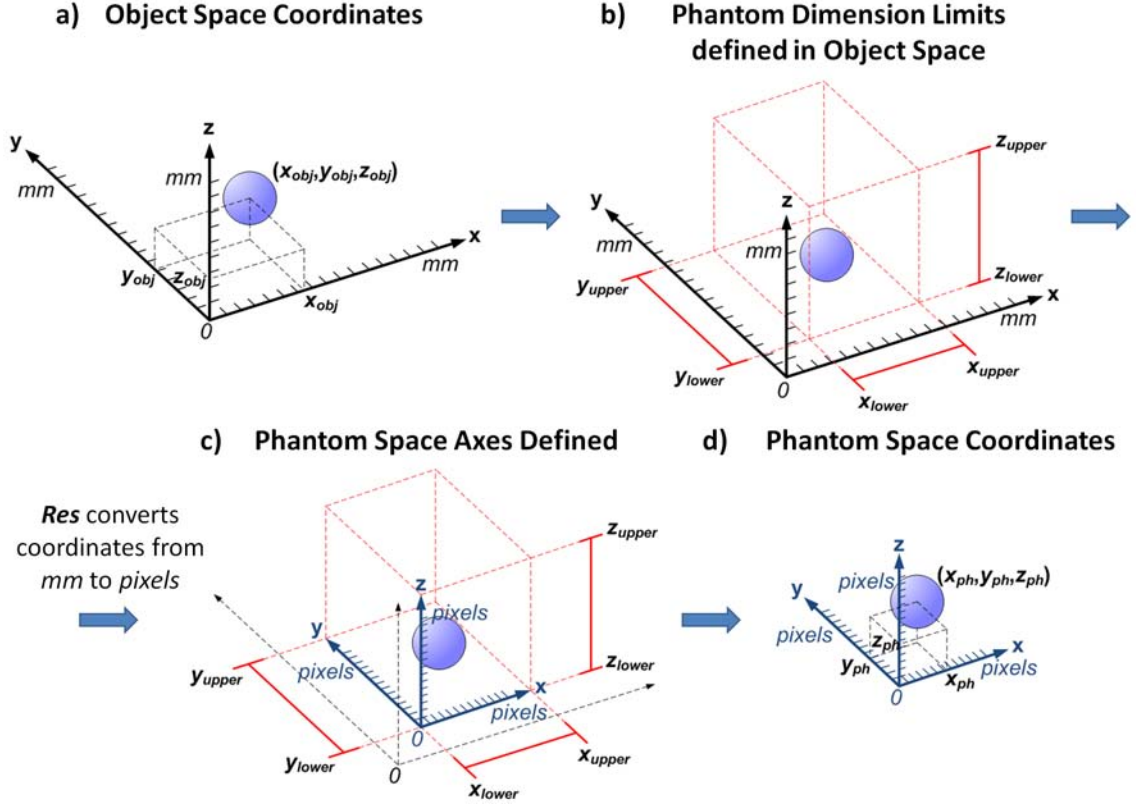


Figure 3.32: The above sequence demonstrates the mapping process from object to phantom space in three-dimensions. (b-c) User defined dimensions and resolution are used to define the new phantom space coordinates (c-d).

where x_{obj} , y_{obj} , and z_{obj} are the object space coordinates (in millimeters) and x_{ph} , y_{ph} , and z_{ph} are the corresponding phantom space coordinates (in pixels). Additionally, dimension measurements, such as radii, must also be converted from millimeters to pixels by

$$r_{ph} = r_{obj} \cdot Res, \quad (3.27)$$

where r_{obj} and r_{ph} represent a radii measurement in object space and phantom space respectively. The equivalent calculation is done for equatorial and polar radii of ellipsoids, etc. These calculations are visualized in the one-dimensional example in Figure 3.33.

3.2.2 Discretization and Tissue Assignment

The phantom matrix is a three-dimensional matrix where each element represents a voxel with center points located at discrete coordinates in phantom space. The representation of volumes from phantom space to discrete voxels in the phantom matrix is called *discretization*. Discretization is

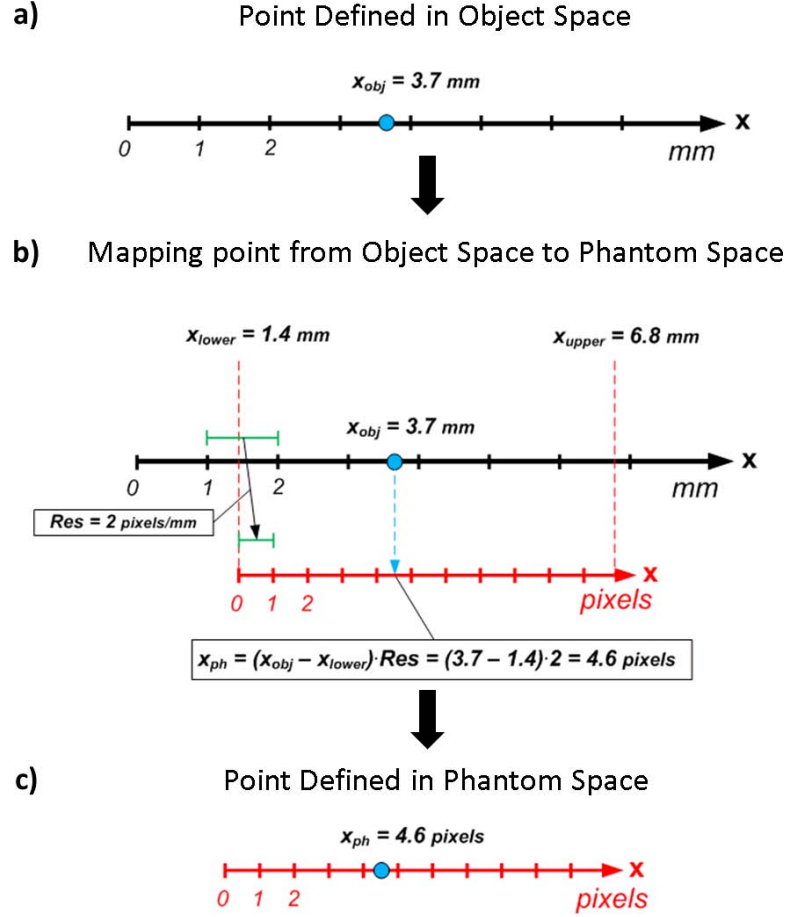


Figure 3.33: 1D example of mapping a coordinate from object space to phantom space using the mapping equation from Equation 3.26.

essential to represent that phantom digitally for visualization and image simulation purposes. The size of the phantom matrix is determined by the object space dimension limits and resolution as

$$\begin{aligned}
 N_x &= \text{floor}((x_{\text{upper}} - x_{\text{lower}}) \cdot \text{Res}) \\
 N_y &= \text{floor}((y_{\text{upper}} - y_{\text{lower}}) \cdot \text{Res}) \\
 N_z &= \text{floor}((z_{\text{upper}} - z_{\text{lower}}) \cdot \text{Res})
 \end{aligned} \tag{3.28}$$

where N_x , N_y , and N_z are lengths (in pixels) of the matrix in the x -, y -, and z - directions respectively. Because N_x , N_y , and N_z must be discrete integers, their values are rounded down to the nearest integer value.

Each element in the matrix is a voxel that represents the phantom volume at discrete coordinates as shown in Figure 3.34. The values of each voxel are chosen to represent different tissues of the phantom. Thus, each voxel is assigned an integer value that represents a specific tissue type (i.e.

Adipose = 1, Fibrous = 2, Glandular = 3 and No Tissue = 0). Through discretization, we determine the tissue type of each voxel from the volume representations in phantom space.

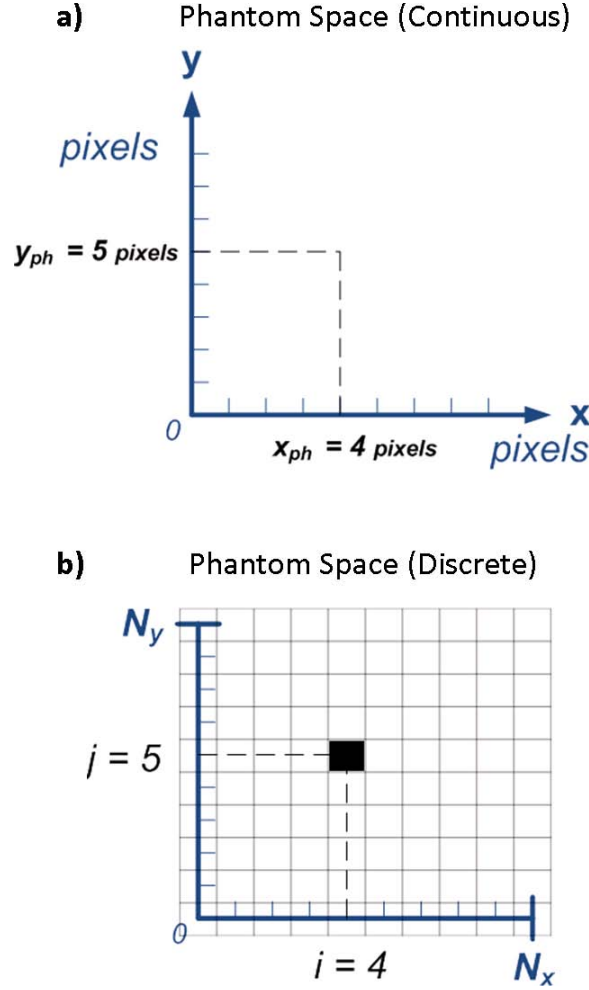


Figure 3.34: The above is a 2D example of how (a) phantom space is discretely represented by the (b) phantom matrix via discretization. The discrete coordinates in phantom space correspond to the individual elements of the phantom matrix. The value of the phantom matrix element is dependent on the discrete coordinate in phantom space that it represents.

A two-dimensional example shown in Figure 3.35 helps to describe this method. Given a geometric object in object space (Figure 3.35a-b), the equivalent coordinates and dimensions (i.e. radius) are calculated in phantom space, converting measurements from millimeters to pixels (Figure 3.35c-d). The discrete coordinates in phantom space, which represent voxels in the phantom matrix, are each examined to determine the tissue type of the corresponding voxel based on the *assignment condition* of the geometric object. An assignment condition of a geometric object determines the tissue types assigned to certain points. For example, the assignment condition of an adipose sphere assigns all points encompassed by the sphere as adipose tissue and all other points unchanged.

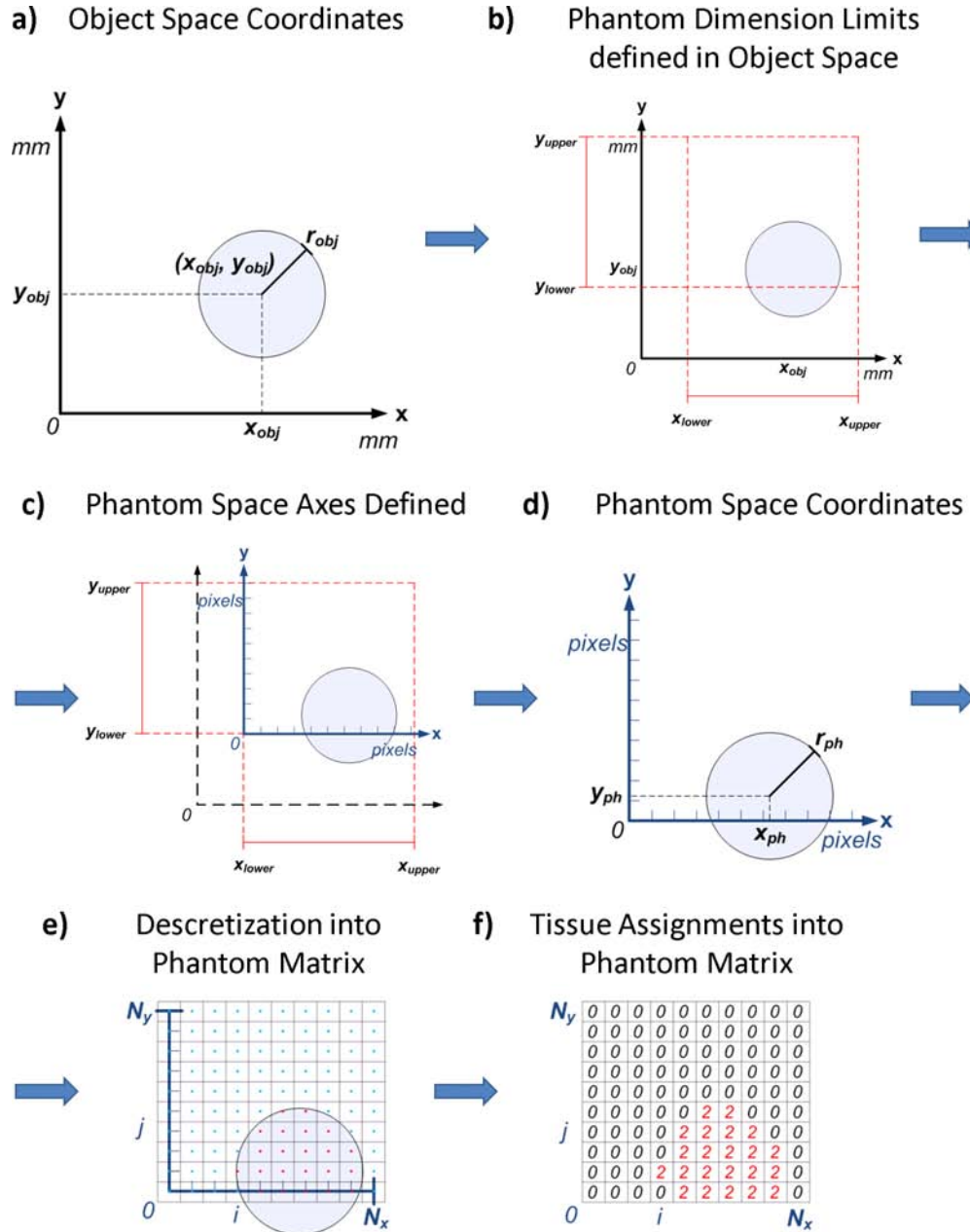


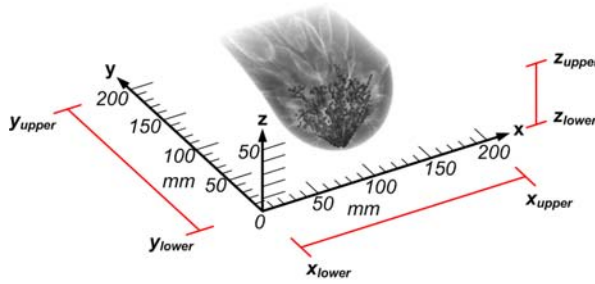
Figure 3.35: Above is a mapping and discretization example for the 2D case. (a) The original object exists in object space as a circle with radius, r_{obj} . (b) The desired dimensions and resolution are user defined, (c) the phantom space axes are defined, and (d) the object is mapped into phantom space. (e) The discrete coordinates of phantom space are examined for tissue assignment and (f) the appropriate integers representing tissue types are placed into the phantom matrix.

The tissue assignment for each voxel is made based on the discrete coordinate point in phantom space representing each voxel, as demonstrated in Figure 3.35e (i.e. If the discrete coordinate point satisfies the assignment condition, the corresponding voxel is assigned as that tissue type). The equivalent is done in three-dimensions for the phantom matrix. Here, we define the object to be a fibrous circle, thus pixels with center points within the radius of the circle are assigned an integer value of 2, which corresponds to fibrous tissue (Figure 3.35f).

Completing this procedure for all geometric objects for each structure representing the breast completes discretization of the breast phantom. The resulting phantom matrix is a discrete breast tissue map for defined dimensions and resolution of a continuous breast object. Figure 3.36 demonstrates the mapping and discretization for two different examples. The first example in Figure 3.36a creates a phantom that represents the complete volume dimensions (200 x 200 x 50 mm) with a course resolution of 1 pixels/mm. This creates a phantom matrix of size 200 x 200 x 50 pixels with pixel size of 1 mm. The second example in Figure 3.36b creates a smaller dimension phantom (100 x 100 x 25 mm) with a finer resolution of 2 pixels/mm. This also happens to create a phantom matrix of size 200 x 200 x 50 pixels but with pixel size of 0.5 mm. This demonstrates how phantoms of different volume dimensions and resolution can be generated.

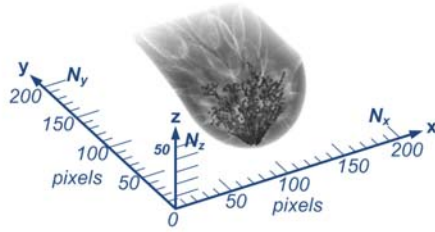
a) Dimensions: 200 mm x 200 mm x 50 mm
(x_{lower} , y_{lower} , z_{lower}): (0, 0, 0)
(x_{upper} , y_{upper} , z_{upper}): (200, 200, 50)

Resolution: 1 pixels/mm



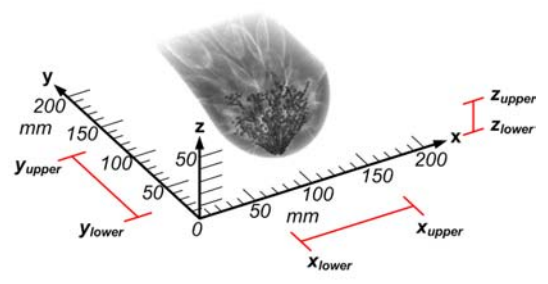
Mapping &
Discretization

$$\begin{aligned} N_x &= \text{floor}((x_{upper} - x_{lower}) \cdot \text{Res}) = (200 - 0) \cdot 1 = 200 \text{ pixels} \\ N_y &= \text{floor}((y_{upper} - y_{lower}) \cdot \text{Res}) = (200 - 0) \cdot 1 = 200 \text{ pixels} \\ N_z &= \text{floor}((z_{upper} - z_{lower}) \cdot \text{Res}) = (50 - 0) \cdot 1 = 50 \text{ pixels} \end{aligned}$$



b) Dimensions: 100 mm x 100 mm x 25 mm
(x_{lower} , y_{lower} , z_{lower}): (50, 25, 0)
(x_{upper} , y_{upper} , z_{upper}): (150, 125, 25)

Resolution: 2 pixels/mm



Mapping &
Discretization

$$\begin{aligned} N_x &= \text{floor}((x_{upper} - x_{lower}) \cdot \text{Res}) = (150 - 50) \cdot 2 = 200 \text{ pixels} \\ N_y &= \text{floor}((y_{upper} - y_{lower}) \cdot \text{Res}) = (125 - 25) \cdot 2 = 200 \text{ pixels} \\ N_z &= \text{floor}((z_{upper} - z_{lower}) \cdot \text{Res}) = (25 - 0) \cdot 2 = 50 \text{ pixels} \end{aligned}$$

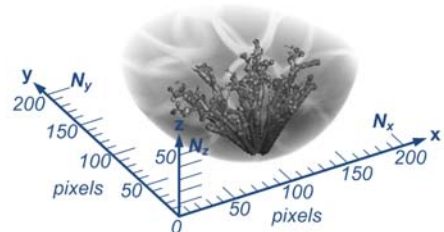


Figure 3.36: Mapping and discretization of different dimensions and resolutions. (a) The first example creates a phantom that represents the entire volume dimension of 200 mm x 200 mm x 50 mm and a coarse resolution of 1 pixels/mm. (b) The second example creates a phantom that represents volume dimensions of 100 mm x 100 mm x 25 mm with a finer resolution of 2 pixels/mm.

Chapter 4

Results

4.1 Image Modality Simulations

After generating the breast phantom, voxel values are converted from tissue representing integer values to biophysical parameters that represent tissue properties that interact with the energy of the imaging modality being simulated. Imaging modalities produce contrast via physical interactions that can be quantified by physical parameters. For x-ray mammography and computed tomography (CT), linear attenuation coefficients of tissues produce contrast through the attenuation of x-ray photons that pass through the body before reaching a detector. For ultrasound, spatial variations in acoustic impedances within tissues scatter transmitted sound waves.

4.2 Mammography

4.2.1 Mammography Simulation

In mammography, a beam of x-rays or photons with mammographic level energies are emitted from an x-ray tube towards the breast. Physical interactions between the tissue and incident x-rays cause some x-rays to lose energy, and change direction (scattering) or be absorbed completely, while some continue to pass through and interact with the detector. The result is a reduction in photon fluence. The x-rays that pass through the object are detected by a two-dimensional array of detectors and counted. This value yields the quantity of *relative exposure*.

The number of x-rays that are effectively absorbed by tissue is determined by its *linear attenuation coefficient*. The linear attenuation coefficient is calculated by a tissue's mass attenuation coefficient and density. The mass attenuation coefficient has units mm^2/g and is dependent on the tissue type and x-ray energy, meaning the mass attenuation coefficient of a specific tissue is different for each energy. The tissue density has units g/mm^3 and is dependent on the tissue. Tissue density can vary greatly depending on its location, distribution and function. For the scope of this project,

we assume a uniform tissue density for all tissue types based on their calculated average tissue density. The linear attenuation coefficient of a tissue for a particular energy has units mm^{-1} and is calculated as the respective mass attenuation coefficient multiplied by tissue density.

The effect of linear attenuation coefficients on incident x-rays can be illustrated by Beer's Law equation

$$N(L) = N_0 e^{-\mu L} \quad (4.1)$$

where N_0 is the number of incident x-rays, μ is the effective linear attenuation coefficient, L is the distance traveled through the tissue, and N is the number of x-rays that pass through the tissue. In the instance of x-rays traveling through different distances x_i and encountering tissue with varying attenuation μ_i , Equation 4.1 changes to

$$N = N_0 e^{-\sum_i \mu_i x_i} \quad (4.2)$$

where $\sum_i x_i = L$.

The typical mean photon energy used in mammography is approximately 20 keV, thus we use this energy in our simulations. The photon absorbers present in our phantom are adipose, fibrous, glandular, and air. Mass attenuation coefficient values and densities of these tissues are gathered from the International Commission on Radiation Units and Measurements (ICRU) [30]. Values for breast fibrous and glandular tissue were not specifically available from ICRU, thus values of muscular fibrous tissue and breast tissue were used for fibrous and glandular tissue, respectively. Table 4.1 shows the mass attenuation coefficients, average densities, and calculated linear attenuation coefficients for each tissue at 20 keV.

Mass Attenuation Coefficients and Densities

<i>Tissue</i>	<i>Mass Attn. Coeff. @ 20 keV (mm^2/g)</i>	<i>Avg. Density (g/mm^3)</i>	<i>Linear Attn. Coeff. (mm^{-1})</i>
Adipose	56.77	9.5×10^{-4}	5.393×10^{-2}
Fibrous	82.05	1.05×10^{-3}	8.615×10^{-2}
Glandular	68.89	1.02×10^{-3}	7.036×10^{-2}
Air	77.68	1.20×10^{-6}	9.3215×10^{-5}

Table 4.1: Mass attenuation coefficient and density values gathered from ICRU [30]. Linear attenuation coefficients are calculated by multiplying mass attenuation coefficient and density.

Voxel values of the phantom are converted to appropriate linear attenuation coefficients. This results in a three-dimensional linear attenuation map that can now be processed for mammography

simulation. A volume of the complete breast phantom is 100 x 200 x 50 mm in the x -, y -, and z - directions, respectively, and the photons are counted with a spatial sampling of 100 μm . Our breast phantom is uncompressed, however in mammography it is common to compress the tissue to create a uniform tissue thickness and reduce dynamic range for imaging. Compression of the breast phantom using finite element analysis is an area that can be implemented in future work.

A monochromatic incident x-ray beam of energy 20 keV is simulated. The incident number of x-ray photons is selected as $N_0 = 6 \times 10^{10}$. This number is derived from typical exposure levels in mammography. For simplification and memory issues, parallel beam geometry is assumed. To generate medio-lateral projected mammograms (projection along the x -axis), the linear attenuation map is summed along the x -direction as described by Equation 4.2. Here, we know the sampling increment for each voxel is 100 μm . This results in a two-dimensional image that is 200 x 50 mm sampled at $x_i = 100 \mu\text{m}$, where each pixel value is represented as the exponential term, $-\sum_i \mu_i x_i$, from Equation 4.2. To generate the number of transmitted x-rays, or relative exposure, N , we can simply apply Equation 4.2 where $N_0 = 6 \times 10^{10}$ to each pixel.

In digital x-ray, relative log exposure values are typically mapped to what is called an *optical density characteristic curve* to create an image similar to that of a classical film x-ray system. The characteristic curve is shown in Figure 4.1 where the log exposure values on the x -axis are mapped to the appropriate optical density values, which are then translated into gray-scale values. Optical density is shown on the left y -axis and is a value that relates to the brightness of an x-ray film. The corresponding gray-scale values are shown on the right y -axis and are the values of brightness in digital x-ray. The largest optical density occurs at the top part of the characteristic curve and corresponds to the darkest (minimum) gray-scale value. The lowest optical density occurs at the bottom part of the characteristic curve and corresponds to the brightest (maximum) gray-scale value. This means pixels detecting more photons (less attenuation) are darker while pixels detecting fewer photons (greater attenuation) are brighter. The relative log exposure is calculated by taking the log of the number of x-rays detected at each pixel. This value is then normalized over the x -axis so that the highest exposure value is located at the base of the top curve and the lower exposure value is located at log 0.5 greater on the x -axis than the bottom curve as illustrated in Figure 4.1.

4.2.2 Mammography Analysis

For our mammography studies, we generated uncompressed, medio-lateral mammograms of multiple phantoms of four different adipose tissue percentages of 40%, 50%, 60%, and 70%. Four resulting

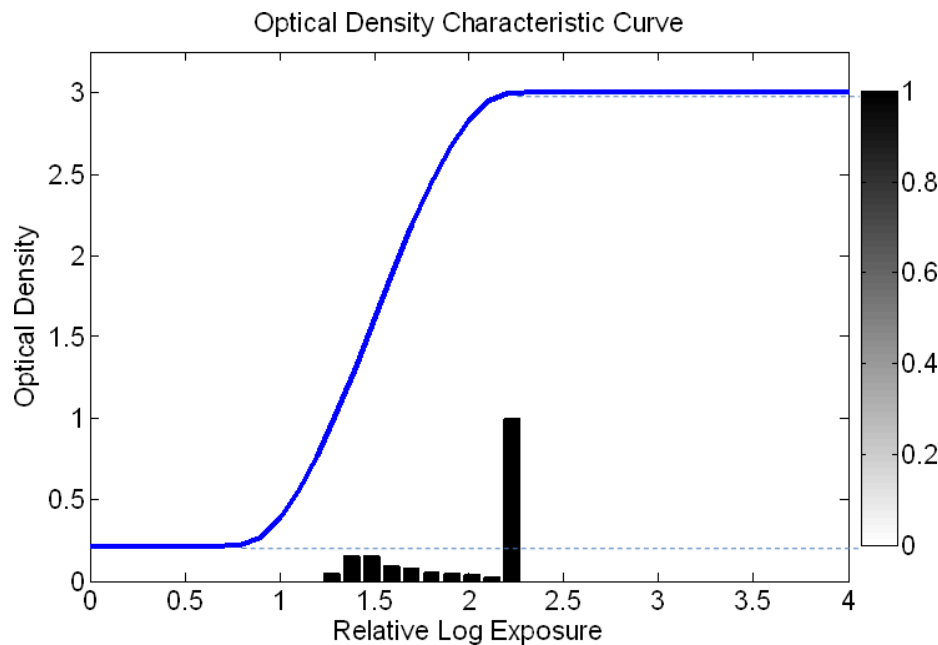


Figure 4.1: The optical density characteristic curve is used to map relative log exposure values to gray-scale values shown on the right.

mammograms from each percentage are shown in Figure 4.2.

Structural features apparent in the simulated mammograms can be easily recognized. The subcutaneous and retromammary fat layers can be seen as the lesser attenuating borders of the breast. Cooper’s ligaments can also be identified within these fat layers as brighter thin bands. Ducts and lobules are not visible as their attenuation is very similar to fibrous tissue and do not produce enough contrast to be visible.

Variances between simulated mammograms due to different adipose tissue percentages are evident. As the phantom increases in adipose percentage, the brightness in the fibroglandular region of the image is reduced. The increased adipose content of the phantom causes less attenuation, thus more exposure at the detector, resulting in a darker image. Additionally, the increased number of adipose compartments increases the gray-scale value variance and produces random areas with varying amounts of attenuation, resulting in an image that appears to have greater “texture”.

Comparing simulated mammograms to the clinical mammogram in Figure 4.2e, the overall contrast and texture appear similar. In general, larger scale features in both appear similar including the subcutaneous fat layer, fibroglandular region, Cooper’s ligaments, and varied distribution of adipose. In the clinical mammogram, it appears as though more intraglandular fat is localized in the outer boundaries of the fibroglandular region, while intraglandular fat is distributed randomly within our phantom. With further examination, a more anatomically accurate method of modeling

and placing intraglandular fat within the breast could be proposed and developed in the future.

Also noticeable is that simulated mammograms lack the detail that clinical mammograms display when both are examined at finer resolutions. This is most likely due to the lack of varying tissue distribution and densities, as well as lack of a method to model structures at finer resolutions within the phantom. Further development in this area would hopefully better simulate the smaller features present in clinical mammograms within our simulated mammograms. Another area of improvement for the simulation would be to simulate a polychromatic x-ray beam, cone beam geometry and implement a compression model. This is more similar to what is done clinical and would result in a more realistic simulation.

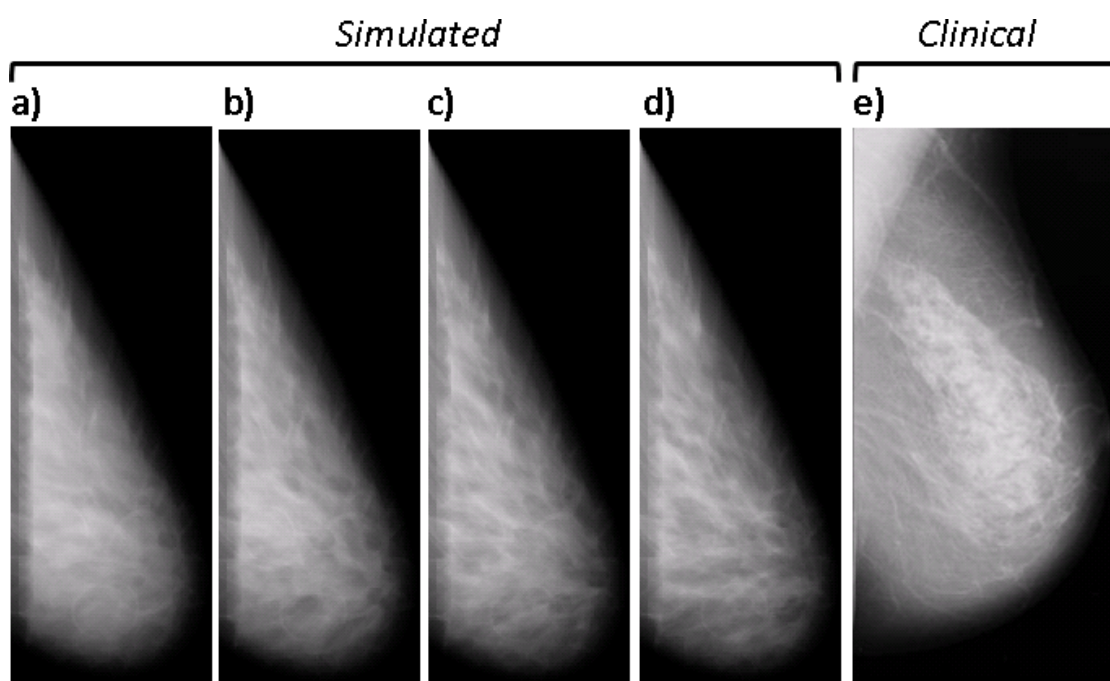


Figure 4.2: a-d) Simulated mammograms for different adipose percentages: 40%, 50%, 60%, and 70%. e) Clinical mammogram. (Clinical mammogram used with permission from Bliznakova et al [5].)

The texture of our simulated mammograms is validated through fractal analysis. Fractal analysis is performed on simulated mammograms and compared to fractal dimension (FD) values obtained from clinical and simulated mammograms in the literature [3, 6, 7, 18]. The fractal dimension of an image or texture measures how completely the structure fills the tissue space as one changes spatial scales. These structures do not fill the complete volume (Fractal Dimension = 3), nor are they confined to a plane (Fractal Dimension = 2). Therefore, we expect the fractal dimension to have a value between 2 and 3.

The fractal dimension is calculated from each mammogram using a similar method as described by Tourassi et al [29]. To do so, a region of interest is selected that contains the fibroglandular region. The 1D radially averaged power spectrum of this region is calculated and plotted on a log – log scale. An example showing the fibroglandular region of a mammogram and the resulting radially averaged power spectrum is shown in Figure 4.3. The fractal dimension can be extracted by applying a linear regression to fit the linear region of the power spectrum and taking the absolute value of the slope as the fractal dimension. This method is applied to each simulated mammogram, fractal dimensions are statistically analyzed, and the results are shown in Table 4.2.

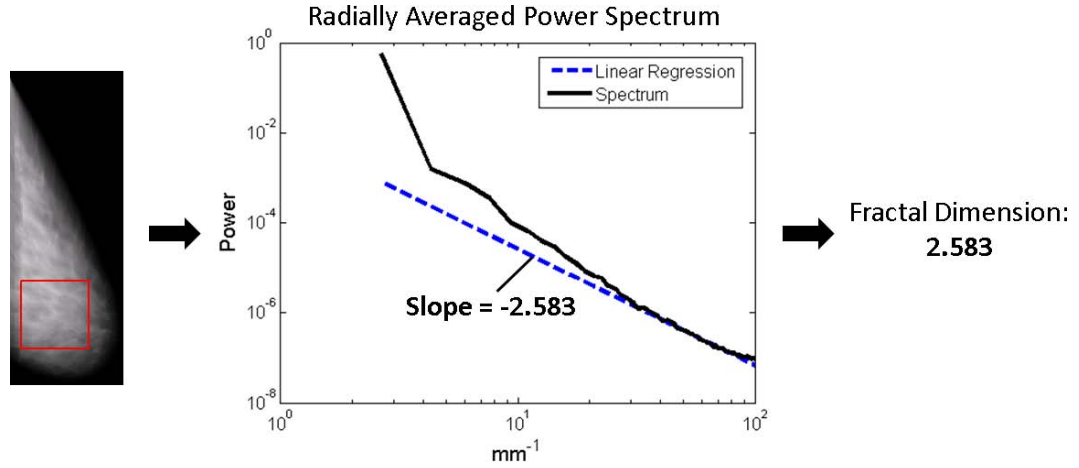


Figure 4.3: (Left) Mammogram with highlighted parenchyma region. (Center) Radially averaged power spectrum of the mammographic fibroglandular region and corresponding linear regression with slope. (Right) Fractal dimension is calculated as the absolute value of the linear slope.

Fractal Dimension Results

<i>Simulated Mammograms</i>	<i>Fractal Dimensions</i>
40% A, 60% FG	2.504 ± 0.026
50% A, 50% FG	2.534 ± 0.0026
60% A, 40% FG	2.568 ± 0.001
70% A, 30% FG	2.584 ± 0.0015

Table 4.2: Fractal dimensions of mammograms with different adipose/fibroglandular tissue percentages.

These results agree overall with fractal dimensions of mammograms found in literature. Calculated fractal dimensions of both clinical and simulated mammograms from different sources in the literature are shown in Table 4.3. While our values are slightly higher than those in literature, the fractal dimension values are very stable and agree with trends found in other studies. It is also interesting to note that as the adipose percentages present in the breast increase, the fractal dimension values increase as well. This correlation is also supported in the study by Tourassi et

al [29]. It can be concluded that the fractal dimension results in our study agree with the calculated fractal dimensions of other sources for both clinical and simulated mammograms. Therefore, we can use this as a source of validation for both our phantom and mammography simulation.

Clinical and Simulated Fractal Dimension Results from Literature

<i>Clinical/Simulated Mammograms</i>	<i>Study</i>	<i>Fractal Dimensions (Mean \pm SD)</i>
Clinical	Caldwell [7]	2.29 ± 0.06
Clinical	Byng [6]	2.39 ± 0.11
Simulated	Bakic [3]	2.39 ± 0.10
Simulated	Li [18]	2.425 ± 0.18

Table 4.3: Fractal dimensions of clinical and simulated mammograms from different studies.

4.3 Ultrasound

4.3.1 Ultrasound Simulation

Ultrasound images or *sonograms* are generated by first selecting a two-dimensional region of interest within a slice of the breast phantom. For our simulation, we use a sagittal slice passing through the center of the breast for the scanning plane. We then select a region of interest with dimensions 42 x 25 mm in the axial and lateral directions respectively, and 100 μm pixel size. The region of interest is oriented at an angle to have an approximately flat surface perpendicular to the axial scanning direction. The pixel values of this region of interest are reassigned with the appropriate acoustic impedance values found from literature [22]. Impedance values are shown below in Table 4.4. This creates a two-dimensional object acoustic impedance map. An example of the sagittal slice and region of interest is shown in Figure 4.4.

Acoustic Impedance Values

<i>Tissue</i>	<i>Impedance (MRayl)</i>
Adipose	1.45
Fibrous	1.80
Glandular	1.54
Air	≈ 0

Table 4.4: Acoustic impedance values of different tissues [22].

Field II [15, 16] is used to numerically generate a pulse with transducer properties of a Siemens Antares system. Transducer parameters include 20 mm *tx/rx* apertures, linear array aperture geometry and $f/2$ in-plane and $f/4$ elevational focusing. Point scatterers are added to different regions

of the impedance map according to their average histological cell densities. B-mode images are then created from the echo signals by computing the envelope of the analytic signal. The attenuation factor equation $e^{-\alpha_0 f d}$ is applied with coefficient $\alpha_0 = 0.5\text{dB/cm} \cdot \text{MHz}$, axial depth d cm and frequency $f = 7$ MHz. After demodulation, time-gain compensation and log compression are applied. The images are then smoothed using a 7×7 pixel kernel median-filter to reduce speckle contrast. An example result of this simulation is shown in Figure 4.4 which shows the region selected as the impedance map and the corresponding generated sonogram.

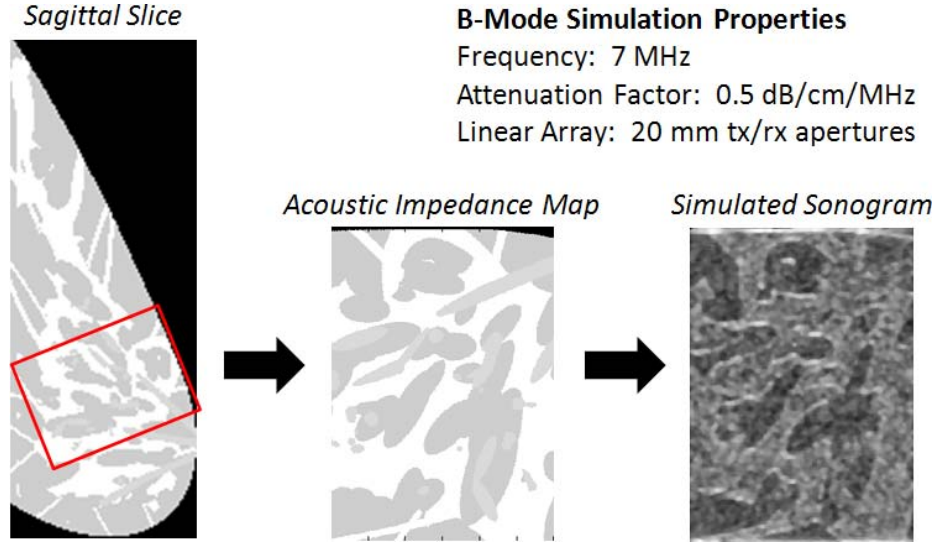


Figure 4.4: (Left) Sagittal slice with selected region of interest, (center) acoustic impedance map and (right) respective simulated sonogram.

4.3.2 Ultrasound Analysis

Sonograms are simulated from phantoms of four different adipose tissue percentages: 40%, 50%, 60%, and 70%. Simulated and clinical sonograms are shown and compared in Figure 4.5. The simulated imaging surface does not appear completely flat because we are not attempting to model a transducer compressed against the skin and instead assume the area outside of the breast to have 0 MRayl impedance.

Structural features within the simulated sonograms can be recognized. The outer skin surface has a brighter, echogenic boundary followed by a darker, hypoechoic underlying layer corresponding to subcutaneous fat. Cooper's ligaments can be seen as thin bright segments located within the subcutaneous fat layer. The subcutaneous-fibrous surface and fibroglandular region is displayed as the brighter region below the subcutaneous fat layer. It is noticeable that as the amount of intraglandu-

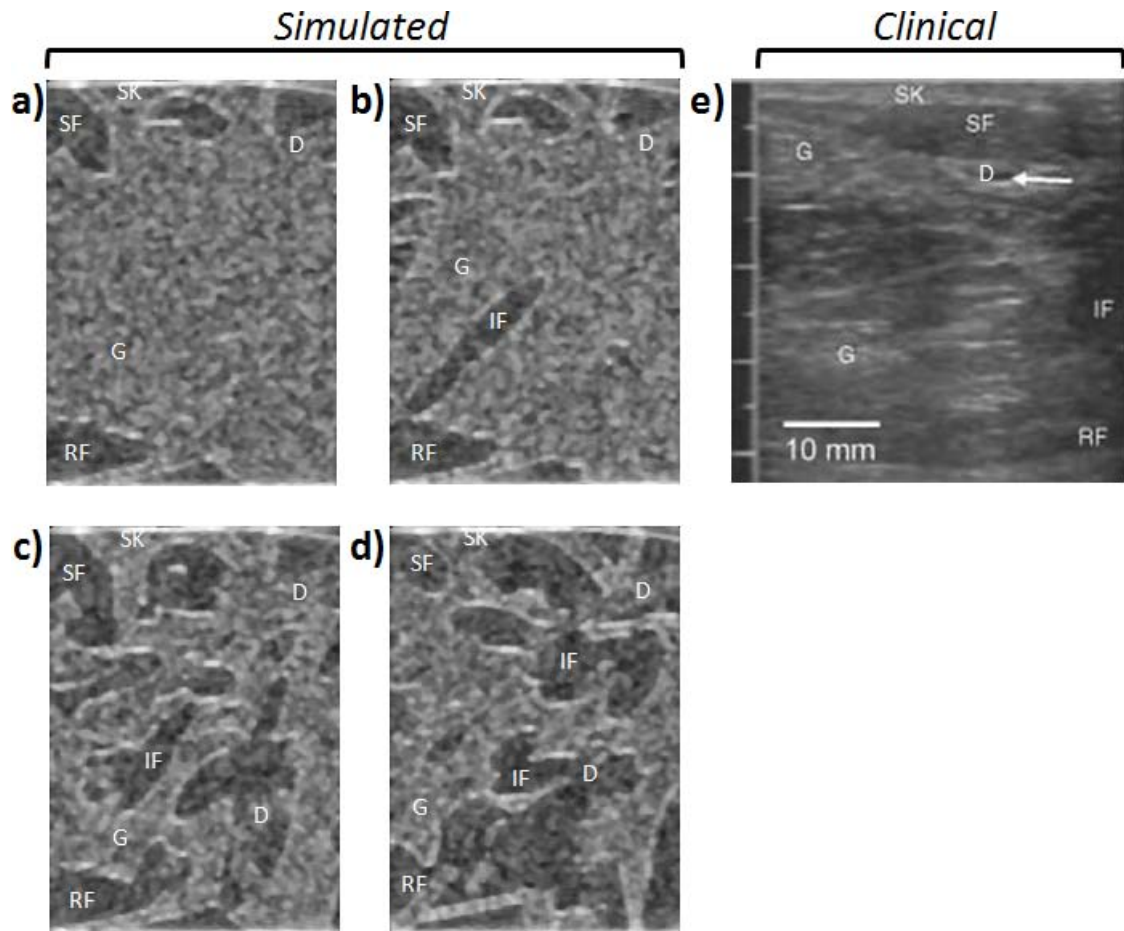


Figure 4.5: a-d) Simulated sonograms for different adipose percentages: 40%, 50%, 60%, and 70%. e) Clinical sonogram where SK = Skin, SF = Subcutaneous Fat, G = Fibroglandular (Fibrous), IF = Intraglandular Fat, D = Ductal Tissue (Glandular), and RF = Retromammary Fat. (Clinical sonogram used with permission from Ramsay et al [26].)

lar fat increases, more dark compartments within the fibroglandular region appear. Ductal branches can be identified as thin bands within the fibroglandular region that are brighter than adipose tissue and slightly darker than fibrous tissue.

Comparing simulated and clinical sonograms in Figure 4.5, the speckle sizes appear similar, though the clinical speckle is less pronounced due to filtering, suggesting that the simulated beam properties are similar to clinical values. Simulated and clinical pixel intensities of adipose and fibrous tissue appear consistent in that their values and contrast between adipose and fibrous tissue are approximately equal in both cases. In the clinical sonogram, ductal branches appear having brighter echogenic boundaries and darker hypoechoic centers. Ductal branches in simulated sonograms appear bright throughout the ductal tissue and harder to differentiate from fibrous tissue. This may be because the cell density for ductal branches varies spatially which is not accounted for in our simulation or that our cell density estimation is not accurate. Another cause may be due to the fact that the clinical sonogram is of a lactating breast as opposed to normal. The location and distribution of features appear similar. The orientations of intraglandular fat differ, however it is difficult to compare due to the unknown region of interest of the clinical sonogram. Cooper's ligaments appear more prolific in the simulated sonogram, which may suggest our simulated Cooper's ligaments are too thick and their estimated density is too large. It is also difficult to verify that the overall tissue distributions present in the clinical sonogram are equivalent to the phantoms being simulated. This is due to the unknown region of interest in the clinical sonogram where the tissue distribution within the breast can vary from region to region.

Examined at a smaller scale, the simulated sonogram tissue structures appear somewhat inconsistent with what is shown in clinical sonograms where boundary surfaces appear more rigid in the simulated sonograms. The most likely cause of this difference is a lack of a model to simulate tissue distribution and cell densities at smaller scales. By modeling only large-to-medium scale structures and assuming uniform cell densities, features at finer resolutions appear more rigid. The sharp cutoffs of geometric objects can result in scattering that looks less organic. Further development in this area is needed and could be made by applying known anatomical knowledge at the 10-100 μm scale to create a more accurate model. Furthermore, sonogram simulation could be used as a feedback tool to develop a more realistic model at these scales for other imaging modalities.

4.4 Computed Tomography

4.4.1 Computed Tomography Simulation

Computed tomography (CT) images are acquired through the coronal plane of the breast phantom. In our simulation, coronal slices are taken halfway between the nipple and chest wall at 25 mm depth. The total slice area selected has dimensions 100 x 100 mm in the xy -plane and 250 μm pixel size. Because the outermost skin layer was not simulated in the phantom but does appear in CT images, an approximate 0.5 mm thick layer of fibrous tissue is added to the breast boundary in the phantom slice. The same mass attenuation coefficients and uniform tissue densities used in the mammography simulation are assumed, thus pixels are assigned the same linear attenuation coefficient values at 20 keV from Table 4.1 creating a two-dimensional linear attenuation map.

The attenuation map is shown in Figure 4.6a. Using the Radon transform, 180 projections over 180 degrees are acquired from the attenuation map creating a sinogram or “attenuation projection map”. Applying Beer’s law from Equation 4.2 with $N_0 = 6 \times 10^{10}$, the attenuation projection map values are converted to relative exposure values. Next, the log exposure values are mapped to gray-scale values using the characteristic curve from Figure 4.1 in the same manner as the mammography simulation (Figure 4.6b). The image is reconstructed by performing filtered backprojection using a Ram-Lak filter on the gray-scale values to create the simulated CT image (Figure 4.6c). Figure 4.6 shows a visualization of the CT simulation process.

4.4.2 Computed Tomography Analysis

CT simulations are produced from phantoms of four different adipose tissue percentages as in previous simulations: 40%, 50%, 60%, and 70%. A monochromatic beam of energy 20 keV and parallel beam geometry is assumed. The resulting simulated CT reconstructions and clinical CT image are shown in Figure 4.7.

The presence of adipose compartments passing through the coronal CT images is apparent, and it can be seen that they increase in number as the adipose percentage of the phantom is increased. The size variations and random orientations of adipose compartments is also apparent as some adipose areas are larger and elongated compared to others. Ducts and lobules are visible as small spots that appear a bit darker than fibrous tissue, contrary to mammography where ducts are difficult to visualize. Cooper’s ligaments can also be seen in the subcutaneous fat layer extending from the inner fibroglandular region to the outer skin.

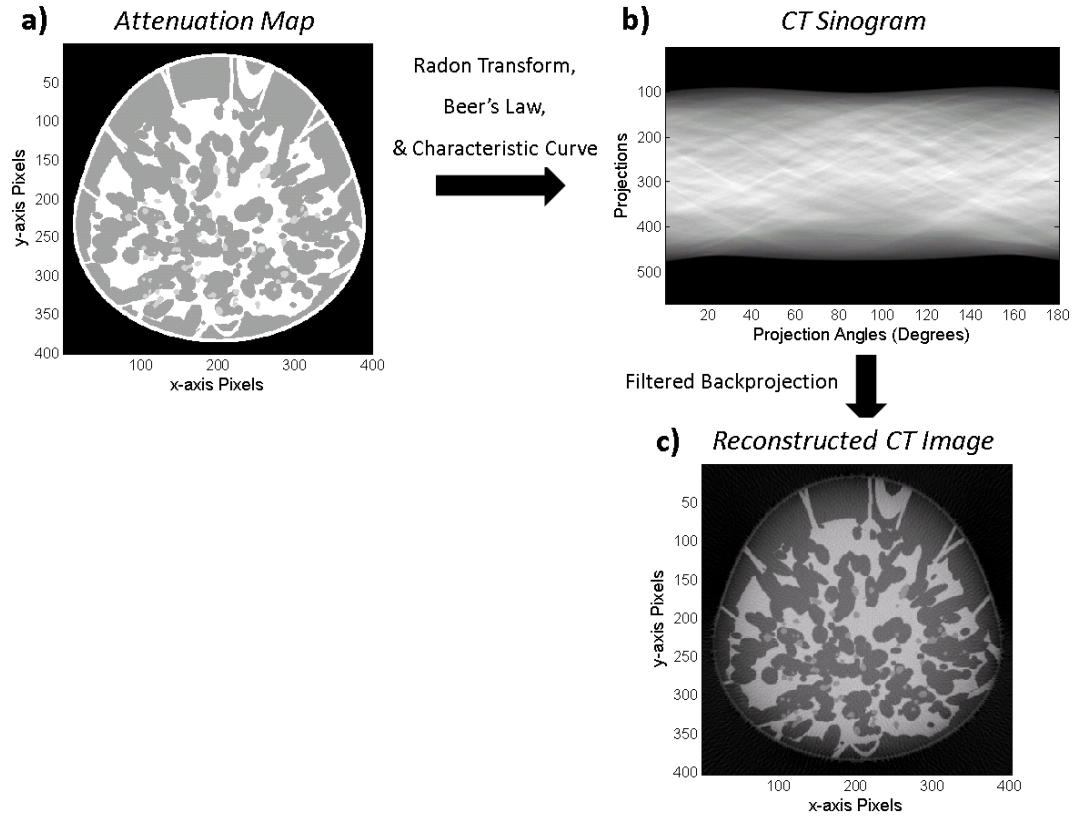


Figure 4.6: Simulated CT Reconstruction. (a) Attenuation map of a coronal slice at 100 x 100 mm dimensions and 250 μm pixel size. (b) CT sinogram after processing by Radon transform, Beer's law, and applying the characteristic curve to generate gray-scale values. (c) Reconstructed CT image using filtered backprojection of sinogram.

The subcutaneous fat layer is apparent in all simulations immediately beneath the outer layer of skin and is structurally the same for each phantom. Realistically, however, the subcutaneous fat layer thickness does change for different breast densities. For instance, the 40% adipose percentage image shows that a majority of the fat present in the corresponding phantom is subcutaneous fat. While this is typically anatomically true, subcutaneous fat thickness would likely be less thick and more intraglandular fat would be present. For more accurate simulations, a model to vary subcutaneous thicknesses based on adipose percentages would be needed.

The tissue distributions in simulated and clinical images appear similar as fibroglandular and adipose “marbling” is present in both. The subcutaneous fat layers are structured similarly in both and have similar irregular surfaces. Cooper's ligaments are also noticeably present in the simulated and clinical images, however these are more pronounced in the simulated images. This observation indicates, similarly with ultrasound results, that the Cooper's ligaments model may be too thick and dense. The intraglandular fat present in the clinical image seems to be located in a more organized

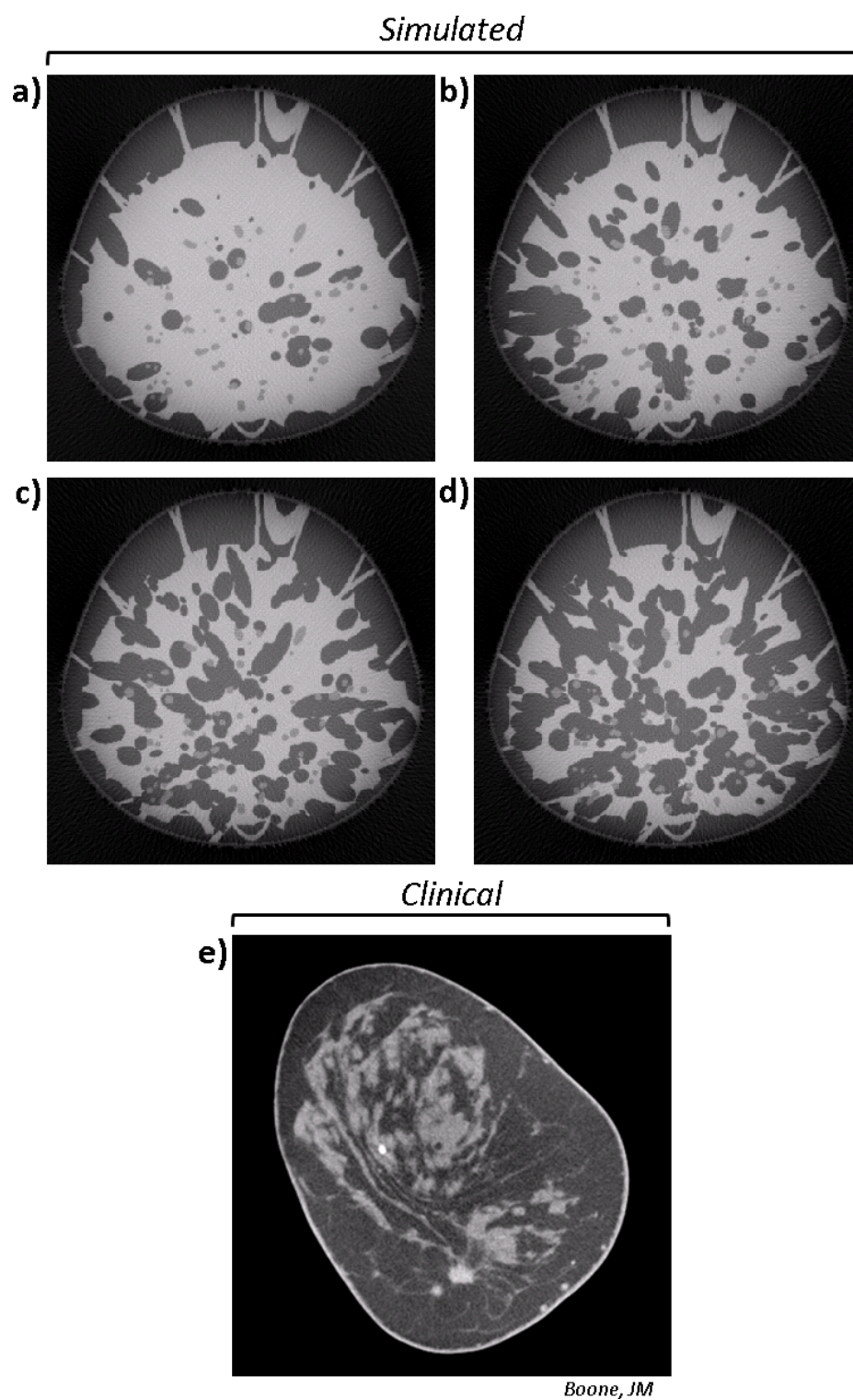


Figure 4.7: a-d) Simulated breast CT images for different adipose percentages: 40%, 50%, 60%, and 70%. e) Clinical breast CT image. (Clinical CT image used with permission from J. M. Boone.)

matter rather than distributed randomly. It tends to be localized more on the outer areas of the fibroglandular region with some centralized fatty deposits. Further analysis of breast CT could yield more insight on how to more accurately model intraglandular fat within the breast.

The fine resolution detail lacking in the simulated images compared to the clinical images is evident, and can be attributed to the lack of a model to simulate accurate tissue distributions and densities at these finer resolutions. As in the ultrasound results, by modeling only large to medium scale structures and assuming uniform tissue densities, image features will tend to appear more rigid and less organic. To solve this problem, more information regarding the tissue distributions and densities at the 10-100 μm scale will need to be examined and a method to model these distributions would need to be further developed and implemented. Comparisons between simulated and clinical CT could provide valuable feedback for this development, resulting in more realistic CT simulations and a more realistic breast phantom as a whole. Another area of improvement for the CT simulation would be to simulate a polychromatic x-ray beam and fan beam geometry. This is more similar to what is done clinical and would result in a more realistic simulation.

Chapter 5

Discussion

5.1 Strengths, Weaknesses and Future Developments

Our project successfully demonstrates a method for constructing an anatomically accurate model of the breast to produce a three-dimensional software phantom. Using this phantom, we were able to simulate multimodality imaging acquisition, including mammography, ultrasound, and CT. There are both strengths and weaknesses to our software phantom and these yield certain advantages and disadvantages for image simulation. The development of the software phantom offers opportunities for a variety of future applications focusing on imaging system development, multimodality imaging techniques, improved feature recognition of images and early cancer detection.

One important strength is the ability to dynamically scale our phantom to desired size dimensions and resolution. When mapping the phantom from mathematical models to a discrete matrix, the represented size and resolution is defined by the user. Because we are mapping mathematical models, the relative locations of structures do not change. Dynamic resolution allows us to adjust the phantom for different imaging modalities that have different sampling rates. Therefore we can adjust the phantom for whatever imaging modality we are simulating and select the dimensions of the region of interest with the appropriate resolution.

By generating a phantom from mathematical models, we are able to alter structures of the breast as we see fit. This enables us to be able to continually produce unique phantoms by randomizing the generation of mathematical models. We can also alter different compositions of the breast according to age and body type. Altering breast composition and structures allows us to develop more robust processing algorithms to work with all types. This method also yields itself towards the adjustment of the mathematical models in the future to improve accuracy. As more detailed anatomical information becomes available and we develop more sophisticated modeling methods, we can easily implement these to produce more accurate phantoms. Additionally, through comparisons between simulated and clinical images, adjustments can be made to the model structure for improved

accuracy and consistency with clinical images. If we had generated our phantom from segmented imaging data, it would not be possible to alter structures from the original imaging data object.

However, a disadvantage to this method is that details of structures are limited to the mathematical model being used. While geometric objects can do a relatively good job at modeling organic structures, at finer resolutions the sharp discontinuities of geometric objects and lack of organic shape can become more apparent. Using segmented imaging data, the tissue distribution is guaranteed to be organic in nature and appear more realistic at finer resolutions. Currently, our use of mathematical models also lacks a method of assigning varying tissue properties. In our mathematical model, geometric objects are assigned mean tissue properties and densities. Using segmented imaging data, it is possible to assign varying tissue properties and densities by inferring these from the pixel values. A solution to this problem would be to continually work to improve the mathematical model at smaller scales, and to develop a method of assigning varying tissue properties and densities based on location and proximity to different tissues and structures.

Another strength is the ability to incorporate new structures into the breast phantom in the future. Currently we focus on a limited number of structures that have been simulated in previous work. We are limited to these due to the lack of anatomical detail on other structures. These include some larger structures such as the pectoral muscle and vasculature. Additionally, incorporating known cell properties and organization within the breast can be used to better model the breast phantom. Histological and FTIR (Fourier transform infrared spectroscopy) samples demonstrating cell distribution within breast tissue are available and future work could possibly incorporate cell distribution models. By continuing to add structures and modeling the breast at smaller scales, the accuracy and validity of the phantom would likely improve as well as create more realistic images at finer resolutions.

An area that can be developed in our mammography and CT simulation is the implementation of a polychromatic x-ray beam, cone beam geometry for mammography, and fan beam geometry in CT. Commonly, a monochromatic beam and parallel beam geometry for such simulations is assumed in literature, however, simulating what is used clinically would likely result in more realistic simulations. Another area that can be incorporated into our mammography simulation is a compression model for use with the phantom. In mammography, it is common to compress the breast for uniform tissue thickness and reduced dynamic range. Some previous software breast phantom models have incorporated this compression model for mammography simulation and have been able to produce more realistic mammograms as a result. We believe this model can be implemented using a finite

element analyzer and known elasticity properties of tissues. Using this type of compression model, we anticipate we would be able to create more realistic mammograms as well.

Another strength of our software phantom is the ability to produce simulated images for multiple modalities. For simulated image acquisition, phantom voxels are assigned appropriate biophysical parameters that interact with energies of the imaging modality being simulated. Simulated images are then produced by applying the corresponding image acquisition model to the processed phantom. The ability to assign these variable biophysical parameters to these models allows the phantom to be diverse and universal to all applicable imaging modalities. Thus, given appropriate biophysical imaging parameters and an accurate imaging acquisition model, simulated images can be produced. This makes the software phantom an attractive tool for use with other imaging modalities in the future.

A major strength of the software phantom is that the object function is known. There are several benefits that a known object function provides us. One is that it ensures that when generating a simulated image that there is never any inconsistent deformation and the imaging environment is always controlled. We can ensure that each simulation is consistent with one another and the only changes are ones we specifically implement in the phantom. This affords us much greater control when attempting to compare images and identify structural changes.

Another benefit of a known object function is that it allows for more convenient image registration. Image registration is the process of transforming different imaging data sets onto one coordinate system. To register two different data sets, one image is typically spatially transformed to align features or intensities with another “reference” image. In clinical imaging, this can prove very difficult due to deformations of the object or subject (i.e. due to a different ROI, repositioning of the object, subject breathing, anatomical changes, etc.). Using the software breast phantom, we can ensure that no deformation will occur and thus making feature alignment much easier. In the event that the object function is transformed for use of imaging simulation (i.e. compression for mammography), it is much easier to transform an image for registration knowing the deformation model used. The benefit of easier image registration will hopefully allow greater examination into multimodality imaging and adaptation into clinical application.

We have been able to validate our mammogram simulations through fractal analysis. However, our ultrasound and computed tomography simulations have only been visually compared with clinical images. While visual comparisons between simulated and clinical images can tell us about image quality, it lacks a method of quantifying how realistic the simulated images are compared to clinical

images. A method to quantitatively compare simulated and clinical images would be necessary to validate other imaging modalities. By incorporating other validation methods, we can improve simulation techniques to produce more realistic images, confirm whether simulated images are realistic, and expand to produce simulations of other modalities.

Modeling tumor growth is a future development area that can be applied to the breast phantom. Literature has shown common locations of ductal carcinoma within the breast as well as models of tumor growth. Adapting these models to our software phantom would allow for the ability to produce phantoms with tumors of different locations, types, and durations of growth. Using these models, it would be possible to custom design new processing methods and multimodality imaging techniques to better resolve tumors within the breast with the goal of detecting tumors earlier.

Another future application area could be the production of realistic simulated images for the use of training radiologists and technologists. As the development of phantom and image acquisition simulation is validated and deemed sufficiently realistic, a training tool to help train clinicians could be developed. By rapidly producing unique images of varying structures and breast composition, radiologists can be trained to recognize features indicative of certain structures and/or tumors. As these features are identified, algorithms could be developed to isolate these features for computer-aided diagnosis. Thus, the breast phantom with modeled tumor growth could provide a very convenient method for improving diagnosis and developing computer-aided diagnosis.

Modeling the inverse of the imaging system is another possible future application. By knowing the underlying input object function, image acquisition system, and resulting output simulated image, it would be possible to model the inverse of the imaging system. The inverse imaging system could effectively produce an estimated object function given a simulated image. Theoretically, with further development of an inverse imaging system and “training” the system to accurately reproduce the original object function from simulated images, object functions could be produced from clinical images. Such application could allow much better estimation of tissue structure, tissue distribution and anatomical detail from clinical images than before.

The development of a three-dimensional in-silico breast phantom is proposed and image simulations are produced and analyzed for multiple imaging modalities including mammography, ultrasound and CT. Strengths of the phantom and areas necessary for improvement are recognized. The strengths of the phantom lie in its dynamic scalability, mathematical modeling method, and known object function. These yield certain advantages for multimodality image simulation, simulating different breast compositions, and imaging system development. Areas needing to be further

developed are detailed tissue properties at smaller scales, improved image acquisition simulation, and incorporating new structures of the breast. By further developing these areas, a more accurate breast model and more realistic simulated images can be produced. There are several potential applications that can be explored with our multimodality software breast phantom including imaging system development, improved diagnosis, and new multimodality imaging techniques. Thus, the goal of the in-silico breast phantom is the improved speed and quality of imaging systems and the earlier detection of cancer.

References

- [1] P. R. Bakic, M. Albert, D. Brzakovic, and A. D. Maidment. Mammogram synthesis using a 3D simulation. I. Breast tissue model and image acquisition simulation. *Med Phys*, 29:2131–2139, 2002.
- [2] P. R. Bakic, M. Albert, D. Brzakovic, and A. D. Maidment. Mammogram synthesis using a 3D simulation. II. Evaluation of synthetic mammogram texture. *Med Phys*, 29:2140–2151, 2002.
- [3] P. R. Bakic, M. Albert, D. Brzakovic, and A. D. Maidment. Mammogram synthesis using a three-dimensional simulation. III. Modeling and evaluation of the breast ductal network. *Med Phys*, 30:1914–1925, 2003.
- [4] P. R. Bakic, M. Albert, and A. D. A. Maidment. Classification of Galactograms with Ramification Matrices. *Acad Radiol*, 10:198–204, 2003.
- [5] K. Bliznakova, Z. Bliznakov, V. Bravou, Z. Kolitsi, and N. Pallikarakis. A three-dimensional breast software phantom for mammography simulation. *Phys Med Biol*, 48:3699–3719, 2003.
- [6] J. W. Byng, N. F. Boyd, E. Fishell, R. A. Jong, and M. J. Yaffe. Automated analysis of mammographic densities. *Phys Med Biol*, 41:909–923, 1996.
- [7] C. B. Caldwell, S. J. Stapelton, D. W. Holdsworth, R. A. Jong, W. J. Weiser, G. Cooke, and M. J. Yaffe. Characterization of mammographic parenchymal pattern by fractal dimension. *Phys Med Biol*, 35:235–247, 1990.
- [8] G. Catanuto, A. Spano, A. Pennati, E. Riggio, G. M. Farinella, G. Impoco, S. Spoto, G. Gallo, and M. B. Nava. Experimental Methodology for Digital Breast Shape Analysis and Objective Surgical Outcome Evaluation. *J Plast Reconstr Aesthet Surg*, 61:314–318, 2006.
- [9] A. Cooper. *The Anatomy and Disease of the Breast*. Lea and Febiger, Philadelphia, Pa, 1845.
- [10] D. T. Geddes. Inside the Lactating Breast: The Latest Anatomy Research. *J Midwifery Womens Health*, 52:556–563, 2007.
- [11] J. J. Going. Ductal-lobar organisation of human breast tissue, its relevance in disease and a research objective: Vector mapping of parenchyma in complete breasts (The Astley Cooper Project). *Breast Cancer Research*, 8:107, 2006.
- [12] J. J. Going and D. F. Moffat. Three dimensional anatomy of complete duct systems in human breast: pathological and developmental implication. *J Clin Pathol*, 49:48–52, 1996.
- [13] J. J. Going and D. F. Moffat. Escaping from Flatland: clinical and biological aspects of human mammary duct anatomy in three dimensions. *J Pathol*, 203:538–544, 2004.
- [14] J. J. Going and T. J. Mohun. Human breast duct anatomy, the ‘sick lobe’ hypothesis and intraductal approaches of breast cancer. *Breast Cancer Research and Treatment*, 97:285–291, 2006.

- [15] J. A. Jensen. Field: A Program for Simulating Ultrasound Systems. *Medical and Biological Engineering and Computing*, 34:351–353, 1996.
- [16] J. A. Jensen and N. B. Svendsen. Calculation of pressure fields from arbitrarily shaped, apodized, and excited ultrasound transducers. *IEEE Trans Ultrason, Ferroelec, Freq Contr*, 39:262–267, 1992.
- [17] N. A. Lee, H. Rusinek, J. Weinreb, R. Chandra, H. Toth, C. Singer, and G. Newstead. Fatty and Fibroglandular Tissue Volumes in the Breasts of Women 20-83 Years Old: Comparison of X-Ray Mammography and Computer-Assisted MR Imaging. *Am J Roentgenol*, 168:501–506, 1997.
- [18] C. M. Li, W. P. Segars, G. D. Tourassi, J. M. Boone, and J. T. Dobbins III. Methodology for generating a 3D computerized breast phantom from empirical data. *Med Phys*, 36:3122–3131, 2009.
- [19] S. M. Love and S. H. Barsky. Anatomy of the Nipple and Breast Ducts Revisited. *Cancer*, 101:1947–1957, 2004.
- [20] E. L. Madsen, M. A. Hobson, G. R. Frank, H. Shi, J. Jiang, T. J. Hall, T. Varghese, M. M. Doyley, and J. B. Weaver. Anthropomorphic breast phantoms for testing elastography systems. *Ultrasound Med Biol*, 32:857–874, 2006.
- [21] E. L. Madsen, J. A. Zaqzebski, G. R. Frank, J. F. Greenleaf, and P. L. Carson. Anthropomorphic breast phantoms for assessing ultrasonic imaging system performance and for training ultrasonographers: part I. *J Clin Ultrasound*, 10:67–75, 1982.
- [22] J. Mamou, M. L. Oelze, W. D. O’Brien, and J. F. Zachary. Perspective on biomedical quantitative ultrasound imaging. *IEEE Signal Processing Magazine*, pages 112–116, May 2006.
- [23] W. B. Nickell and J. Skelton. Breast Fat and Fallacies: More Than 100 Years of Anatomical Fantasy. *J Hum Lact*, 21:126–130, 2005.
- [24] T. Ohtake, I. Kimijima, T. Fukushima, M. Yasuda, K. Sekikawa, S. Takenoshita, and R. Abe. Computer-Assisted Complete Three-Dimensional Reconstruction of the Mammary Ductal/Lobular Systems. *Cancer*, 91:2263–2272, 2001.
- [25] B. Pereira and K. Mokbel. Mammary ductoscopy: past, present, and future. *Int J Clin Oncol*, 10:112–116, 2005.
- [26] D. T. Ramsay, J. C. Kent, R. A. Hartmann, and P. E. Hartmann. Anatomy of the lactating breast redefined with ultrasound imaging. *J Anat*, 206:525–534, 2005.
- [27] J. E. Rusby, E. F. Brachtel, J. S. Michaelson, F. C. Koerner, and B. L. Smith. Breast duct anatomy in the human nipple: three-dimensional patterns and clinical implications. *Breast Cancer Research*, 106:171–179, 2007.
- [28] F. Taneri, O. Kurukahvecioglu, N. Akyurek, E. H. Tekin, M. N. Ilhan, C. Cifter, S. Bozkurt, A. Dursun, O. Bayram, and E. Onuk. Microanatomy of Milk Ducts in the Nipple. *Eur Surg Res*, 38:545–549, 2006.
- [29] G. D. Tourassi, D. M. DeLong, and C. E. Floyd Jr. A study on the computerized fractal analysis of architectural distortion in screening mammograms. *Phys Med Biol*, 51:1299–1312, 2006.
- [30] U.S. National Bureau of Standard. *Report of the task group on reference man: Anatomical values for reference man*, 1975.
- [31] J. J. Vandeput and M. Nelissen. Considerations on Anthropometric Measurements of the Female Breast. *Aesth Plast Surg*, 26:348–355, 2002.

- [32] M. Westreich. Anthropomorphic Breast Measurement: Protocol and Results in 50 Women with Aesthetically Perfect Breasts and Clinical Application. *Plast Reconstr Surg*, 100:468–479, 1997.